Research Square

Preprints are preliminary reports that have not undergone peer review.
They should not be considered conclusive, used to inform clinical practice,
or referenced by the media as validated information.

Out-of-distribution generalization of universal-database models accelerating high-entropy alloy design across the metallic periodic table

Zhen Xie
Fudan University
Jiaxing Chen
Fudan University
Jianqiao Yu
Fudan University
Zonghao Liu
Fudan University
Fan Yang
Fudan University
Ranran Su
Shanghai Jiao Tong University
Hongliang Zhang
Fudan University
Yuexia Wang
yxwang@fudan.edu.cn
Fudan University

Article

Keywords:

Posted Date: November 18th, 2026

DOI: https://doi.org/10.21203/rs.3.rs-11621012/v1

License: This work is licensed under a Creative Commons Attribution 4.0 International License.
Read Full License

Additional Declarations: No competing interests reported.

Out-of-distribution generalization of universal-database models accelerating high-entropy alloy design across the metallic periodic table

Zhen Xie, Jiaxing Chen, Jianqiao Yu, Zonghao Liu, Fan Yang, Ranran Su, Hongliang Zhang, Yuexia Wang**

Z. Xie, J. Chen, J. Yu, Z. Liu, F. Yang, H. Zhang, Y. Wang
Key Laboratory of Nuclear Physics and Ion-beam Application (MOE), Institute of Modern Physics, Fudan University, Shanghai 200433, China
E-mail: Yuexia Wang (yxwang@fudan.edu.cn) | Hongliang Zhang (hlz@fudan.edu.cn)

R. Su
Institute of Nuclear Fuel Cycle and Materials, School of Mechanical Engineering, Shanghai Jiao Tong University, Shanghai 200240, China

Funding: National Natural Science Foundation of China under Grant Nos. 12275055.

Keywords: neural networks, high-entropy alloys, out-of-distribution generalization, universal materials databases, target space partitioning, multi-objective optimization

Abstract

Cost-effective exploration of high-entropy alloys (HEAs) with desired properties remains constrained by scarce HEA property data. We propose a Target Space Partitioning-based Prediction Enhancement Strategy (TSPPES) that enables models pre-trained on universal materials databases to achieve out-of-distribution generalization to compositionally complex HEAs without additional data for training. Coupled with multi-objective optimization, this strategy screens over 10^6 compositions across 60 non-radioactive metals, targeting hardness and thermal conductivity. The models reproduce experimental trends across 6 alloy families and property responses to element addition, removal, or varying content in 4 alloy systems, supporting reliable screening across most of the metallic periodic table. Two W–Re-based HEA families are identified: as-cast $W_{28.63}Re_{14.50}Ta_{28.18}Zr_{14.21}Nb_{14.47}$ (*wt*.%) exhibits a Vickers hardness of 801 ± 9 HV and a total thermal conductivity of 18.00 ± 0.06 $W \cdot m^{-1} \cdot K^{-1}$ at 300 K, while the FCC family member $W_{18.74}Re_{22.31}Pt_{31.55}Pd_{15.30}Ru_{12.10}$ (*wt*.%) combines 816 ± 49 HV with an equivalent room-temperature ductility of ~20%.

Introduction

In recent years, data-driven novel materials design has evolved into a transformative paradigm within materials science research. Materials informatics methods, such as classic machine learning (ML) and deep learning (DL), demonstrate high prediction accuracy, low computational cost, and strong data-mining power [1–3]. These methods provide efficient and powerful tools for diverse applications in materials informatics, including property prediction for high-throughput materials [4–7], composition selection, and optimization [8–10], novel materials generation [11–13], defect analysis [14–16], and intrinsic mechanism analysis [17–19]. Artificial intelligence (AI) algorithms achieve an optimal balance between computational efficiency and accuracy [20], greatly reducing trial-and-error costs for property-driven composition screening [21,22], while shortening the period from materials theoretical design to experimental synthesis [12].

High-entropy alloys (HEAs) have emerged as a transformative class of alloys characterized by their near-equiatomic multi-principal-element compositions that achieve a configurational entropy exceeding 1.61R (R is the gas constant) [23]. This unique feature enables enhanced performance through solid-solution strengthening and cocktail effects, tailoring them for extreme service environments. However, the vast elemental selection space makes high-throughput composition screening of HEAs infeasible through traditional experiments or theoretical calculations. Fortunately, ML-based property prediction has become the dominant methodology for high-throughput HEA composition screening [20–22].

The establishment of the "Composition–Structure–Prediction–Optimization–Experimentation (C–S–P–O–E)" workflow constitutes the core logic for HEA property optimization (Fig. 1a). This workflow has demonstrated remarkable efficacy in optimizing mechanical properties; solving the classical strength–ductility trade-off serves as an exemplary case of multi-objective optimization. In 2020, Zou *et al.* pioneeringly trained an expert and self-learned knowledge enhanced support vector machine model using 44 high-throughput calculated binary Ti-X alloys and 81

experimentally reported alloys. This model predicts the yield strength of Ti-X systems, e.g. the Ti–7Mo–5Al–4Cr–3Ni–0.5Fe–0.2O (*wt.*%) alloy with a yield strength of 1239 MPa and ductility of 8.2% [24]. Notably, Sohail *et al.* identified a HEA with the nominal composition $Fe_{25.3}Ta_{24.8}Ni_{23.9}Co_{19.8}Al_{6.2}$ (*wt.*%), which exhibited a yield strength of 1.8 GPa and remarkable ductility of 25% [25]. Single-objective C–S–P–O–E workflow was also widely used in finding HEAs with ultra-high hardness [26–34]. In 2019, Wen *et al.* employed ML algorithms to develop arc-melted $Co_{26.69}Cr_{35.33}Fe_{8.05}Ni_{6.04}Al_{23.9}$ (*wt.*%) and $Al_{40.95}Co_{23.78}Cr_{20.48}Cu_{5.98}Fe_{6.83}Ni_{5.98}$ (*wt.*%) alloys, achieving a high hardness of 883 HV [26]. Subsequently, Yang *et al.* synthesized $Co_{19.44}Cr_{6.67}Fe_{35.83}Ni_{5.38}V_{32.68}$ (*wt.*%) with an enhanced hardness of 1148 HV [27]. We compile related researches in Table 1. Furthermore, AI-assisted materials optimization and design have been validated in enhancing wear performance [35], tribological properties [36] and creep resistance [10,37,38].

Despite these successes, modern engineering demands—such as those for aerospace and nuclear cladding materials—require multi-functional HEAs that simultaneously satisfy competing structural and functional criteria [39–41]. HEA coatings offer a relevant application scenario because high hardness improves wear resistance, whereas high thermal conductivity suppresses local overheating [42]. Although the present bulk-solid-solution models do not treat coating–substrate interfaces, coating geometries relax bulk-formability constraints and make this property combination practically relevant [43]. However, the AI-assisted optimization and design of multifunctional HEAs still face two key challenges:

(1) High cost of data acquisition. Experimental datasets for HEAs remain constrained to a few hundred data points [24,38,41,44–47], insufficient for robust model training. As an alternative to experiments, first-principles computational results serve as the primary source for high-throughput screening data. However, the calculation cost for given high-entropy alloy properties is prohibitively high. For instance, lattice thermal conductivity (κ_l) is a critical parameter for heat dissipation in accident-tolerant nuclear cladding materials [48]. In HEAs, severe lattice distortion highly scatters electrons, meaning κ_l often dictates the lower bound and accounts for a substantial fraction (>50%)

of the total thermal conductivity [49–53]. Yet, computing κ_l necessitates computation of third-order or higher force constant matrices, which incur substantial computational expense given the compositional complexity of HEAs and the requisite large supercells.

(2) Limited element screening range. Most of property prediction and composition optimization in HEAs depend on compiling limited experimental or computational data of similar system from previous literature, typically constrained to 100-500 data points covering only 5-10 elements (e.g., Al–Co–Cr–Cu–Fe–Ni systems [26]), which severely limits the development of potential novel HEAs, impairing model reliability and training reproducibility, as mentioned in these articles [38,54].

Faced with this data scarcity, researchers must leverage the vast data accumulated in universal material databases. However, generalizing models trained on ordered, simple compounds to the disordered HEA space constitutes a severe out-of-distribution (OOD) problem [55].

To address these bottlenecks, we develop a framework (Fig. 1b) that enables Mix-GNN models (Figs. 2a, b and c) pre-trained on universal materials databases to generalize to disordered HEAs without HEA property data for training. Its core is Target Space Partitioning-based Prediction Enhancement Strategy (TSPPES), which partitions the target space by phase structure and principal-element count, retains subspaces with reliable linear consistency, and excludes unreliable regions. This provides an accessible space of 60 non-radioactive metals; reliability is tested across six representative alloy families and by element addition, removal or content variation in four alloy systems. Using the resulting bulk-modulus and lattice-thermal-conductivity predictors with Nondominated Sorting Genetic Algorithm II (NSGA-II), we screen over 10^6 candidates and identify two W–Re-based families. The as-cast BCC alloy achieves 801.3 ± 9.0 HV and 18.00 ± 0.06 $W \cdot m^{-1} \cdot K^{-1}$ at 300 K, whereas the FCC alloy reaches 816 ± 49 HV with ~20% equivalent room-temperature ductility, suggesting that platinum-group-metal additions can stabilize ductile FCC W–Re solid solutions. Interpretable analyses and feature importance (Figs. 2d, e) further attribute the hardness–thermal-conductivity trade-off to competition among bonding strength, bond density and lattice distortion,

explaining the dominance of refractory compositions. Training and optimization require only a single consumer-grade GPU.

Results

Universal databases provide broad but uneven elemental coverage

Given the scarcity of HEA property data, we trained models on first-principles data from universal materials databases and then generalized them to HEAs. Materials Project (MP) [56] and AFLOW [57] have accumulated 13,172 inorganic-crystal elastic-property entries [58] and 5,652 lattice-thermal-conductivity entries at 300 K [59] , respectively. These databases cover most elements in the periodic table and, in particular, comprehensively cover 60 commonly used non-radioactive metallic elements (Figs. S1a and S2a), including 3*d* transition metals, refractory metals, lightweight metals, rare-earth metals and low-melting-point metals (Supplementary Table S1). Their large data volume and broad elemental coverage provide the basis for training models applicable to HEA discovery. The composition of the metallic subsets is summarized in Supplementary Information Section S1. Of the 12,797 MP entries containing metallic elements, 5,147 are pure metals or alloys and 7,650 are metal-containing compounds. Of the 5,505 AFLOW entries containing metallic elements, 2,196 are pure metals or alloys and 3,309 are metal-containing compounds (Supplementary Figs. S1b and S2b). Most entries in both databases contain fewer than three elements, while quaternary and higher-component entries account for less than 4.0% (Supplementary Figs. S1c and S2c). The two databases therefore provide broad elemental coverage but relatively limited sampling of highly multicomponent alloys.

We therefore trained the models on pure metals, alloys and metal-containing compounds, rather than only on pure-metal and alloy entries. This choice was motivated by three considerations. First, pure-metal and alloy data account for only approximately 40% of the MP and AFLOW data. Training solely on these entries reduces the validation R^2 from 0.8799 to 0.8718 for B and from 0.8720 to 0.8119 for κ_l (Figs. 2f, 2g and Supplementary Fig. S3). Second, several key metallic elements are underrepresented in

pure-metal and alloy data, such as W and Mo in MP and W, Re, Mo and Cr in AFLOW (Supplementary Figs. S1b and S2b) [60]. Incorporating compounds data preserves essential information for these elements. Third, metal-containing compounds and metallic materials share physical relationships governing B and κ_l [61,62], providing useful structure-property information for HEA prediction.

Although including compounds introduces data that are not direct HEA analogues, this noise is addressed by TSPPES, which evaluates model reliability within partitioned HEA subspaces rather than narrowing the elemental search range. The full universal databases are therefore used for training, while only validated subspaces are used for subsequent composition optimization.

Model design and target-space partitioning identify reliable HEA subspaces

For predictive models, we used a joint CGCNN–MLP architecture, Mix-GNN (see Figs. 2a, b and c for details), to combine graph-derived structural representations with composition-, structure- and element-property-based descriptors (see Table S4 and Figs. 2d, e). The main network hyperparameters are listed in Table 2. Mix-GNN achieves validation R^2 values of 0.8799 for MP bulk modulus (Fig. 2f) and 0.8720 for AFLOW lattice thermal conductivity (Fig. 2g), outperforming standalone CGCNN models (0.8234 and 0.7546, respectively, in Fig. S4). Full database training was preferred over pure-metal-only training because it preserves elemental coverage and improves model performance, particularly for sparsely sampled refractory elements. Both bulk modulus and shear modulus were evaluated as candidate mechanical indicators; the bulk-modulus model showed better validation performance (see Fig. 2f) and was therefore used as the core mechanical objective, while bulk modulus has also been widely used as a proxy for hardness. Lattice thermal conductivity serves as a proxy for total thermal conductivity for its dominant position [49].

Feature importance analysis identifies element-weighted melting point, bulk modulus, Young's modulus and atomic-volume descriptors as leading predictors of B, and element-weighted sound velocity, melting point, boiling point and atomic-radius

descriptors as leading predictors of κ_l (Figs. 2d, e). These results connect model predictions to physically interpretable quantities: melting point reflects bonding strength, atomic and cell volumes are related to bond density, and sound velocity and atomic mass affect lattice thermal transport. Complete feature definitions and extraction procedures are provided in Methods and Supplementary Section S4.

In principle, a model trained on universal materials databases should provide accurate predictions for all covered material systems. In practice, model capacity, uneven data availability, limited training time and interference among different material classes prevent such uniform accuracy. Our analysis indicates that perturbations introduced by non-HEA data are confined to specific target subspaces (in Supplementary Information Section 2 and Fig. S5), whereas in other subspaces the interference may be negligible or approximately linear. This makes it possible to identify subspaces in which predicted trends match experimental or DFT references and to perform composition optimization only within these validated regions. Although poorly predicted subspaces are excluded, the retained regions still cover nearly all non-radioactive metallic elements, preserving a broad search space, reducing additional data costs, and improving computation speed for HEA discovery (see Figs. 2h, i, and j). We define the global space as all entries in the universal databases and the target space as single-phase solid-solution medium- and high-entropy alloys. The target space was partitioned by principal-element count and dominant phase into quaternary and quinary FCC and BCC subspaces; the HCP subspace was excluded because of insufficient independent test data. Partitioning at the phase level preserves compositional freedom and allows the composition space to inherit the elemental coverage of the universal databases. Model performance in each subspace was evaluated using r^2 and independent experimental or computational data collected from 178 B and 73 κ_l entries (Supplementary Tables S2 and S3). A one-dimensional polynomial example illustrating the partitioning principle is provided in Supplementary Section S2.

To examine the reliability of the pre-trained models in HEA space, we constructed independent literature-derived pre-testing datasets containing 178 bulk-modulus entries

and 73 lattice-thermal-conductivity entries. These entries were classified by phase structure and principal-element count as well, and model performance in each subspace was evaluated using the linear consistency metric r^2. Unlike R^2 (We have explained the difference between the definitions of r^2 and R^2 in the Methods 1), which can become strongly negative in noisy subspaces, r^2 provides a bounded measure of linear association and is suitable for identifying subspaces with consistent composition–property trends.

All HEA subspaces are evaluated using pre-testing datasets (Fig. 3), and acceptable performance was obtained for B prediction in the ternary FCC (r^2 = 0.8798), quinary FCC (r^2 = 0.9445) and quinary BCC (r^2 = 0.7551) subspaces. For κ_l prediction, the quinary FCC (r^2 = 0.8502) and quinary BCC (r^2 = 0.9433) subspaces met the consistency threshold (marked with red boxes). Subspaces with insufficient pre-testing data or poor linear consistency were excluded from composition optimization. Only the quinary FCC and quinary BCC subspaces, which satisfy the consistency requirements for both B and κ_l, were used for multi-objective optimization. Raw predictions were calibrated using linear relations fitted from the independent pre-testing data within the validated subspaces. The rationale behind TSPPES is that interference from non-HEA entries is not uniformly distributed across the target space, but is concentrated in particular composition and phase subspaces. Subspaces with systematic deviations are excluded, whereas subspaces showing simple linear deviations can still provide reliable relative rankings after calibration. This partitioning-and-calibration procedure defines the optimization domain used in the following section without retraining the models on HEA property data.

Compared with four representative ML-guided alloy-optimization studies, the present framework expands the accessible elemental space to 60 metals, compared with 7–42 elements in those studies [9,63–66] (Fig. 2i). Its principal data-economy advantage is the elimination of newly acquired alloy-specific training data: the models use pre-existing MP and AFLOW entries, whereas previous workflows relied on newly compiled experimental, CALPHAD or high-throughput DFT datasets (Fig. 2h). Training and

optimization were completed on a single NVIDIA RTX 4080 GPU within 120 h, close to conventional small-scale composition search (Fig. 2j).

Composition optimization identifies W–Re-rich alloy families

Owing to the high predictive consistency of B and κ_l in quinary subspaces for both single-phase FCC and BCC HEAs, we optimized their compositions via multi-objective optimization and screened results via the solid solution rules in Method 3. To avoid inefficient searches, we divided the candidate elements into twenty subgroups (listed in Table 3) based on solid solution rules and commonly used metal elements. The detailed division rules were also provided in Methods. NSGA-II optimization converged across the investigated candidate subgroups (Supplementary Fig. S6), and the resulting Pareto-optimal compositions are shown in Fig. 4. As the population evolves, the trade-off between B and κ_l optimizes toward the Pareto frontier. A detailed description of the NSGA-II iterative process and the convergence Pareto front for each sub-candidate element group is provided in Section S5, with corresponding visualizations presented in Figs. S6a and S6b. Compositions with B > 245 GPa and qualified κ_l (> 7.3 $W \cdot m^{-1} \cdot K^{-1}$ for FCC and > 18.0 $W \cdot m^{-1} \cdot K^{-1}$ for BCC) were selected for plotting in Fig. 4a and 4b. Detailed elemental combinations of screened alloys from each subgroup are available in SI Table S5 and S6.

To clarify how individual elements shape the optimized property landscape, the Pareto-optimal quinary populations were projected onto element-fraction-weighted marginal distributions (Fig. 4). In the FCC family, the Os-weighted marginal of B shifts toward higher values, whereas the Ir-weighted marginal peaks at lower B; meanwhile, their κ_l marginals nearly coincide. Os therefore raises B with little penalty in κ_l, while Ir moderates B. In the BCC family, the Mo-weighted marginal develops a pronounced high-B tail beyond 270 GPa that is absent from the Ti-weighted marginal, while Ti-bearing alloys exhibit slightly higher κ_l. These element-specific responses are consistent with the metallurgical roles discussed below. The experimentally validated Pt-1, RE-3

and RE-4 alloys are highlighted in the panels.

Motivated by exploring single-property limits and the need for multi-algorithm cross-validation, we also performed single-objective alloy composition optimization. To keep the main text concise, the unverified screening results and methodological details are provided in the Supplementary Information Section S6 in Fig. S7, while the validation for mechanical properties is presented in Table 4 to enhance algorithmic credibility.

First-principles and experimental validation

To rigorously validate the ML predictions, DFT first-principles calculations were adopted to validate the optimized HEA compositions. All first-principles validation calculations were performed using the unified computational settings described in Methods, consistent with the original material databases. Mechanical properties were acquired via the Vienna Ab initio Simulation Package (VASP) [67] stress–strain method, and lattice thermal conductivity was calculated by combining quasi-harmonic approximation (QHA) [68], the Boltzmann transport [69] and the Slack model [70]. We selected a subset of the predicted compositions for DFT validation mainly based on the model-predicted material performance, solid solution capability, and raw material prices.

This section provides DFT results to verify single-objective B optimization and multi-objective optimization of both B and κ_l. Table 4 lists the optimal alloys from single-objective B optimization, where all alloys meet the Born mechanical stability criteria [71]. We summarized predicted and DFT-calculated bulk modulus, shear modulus, estimated Vickers hardness, Pugh's ratio and Poisson's ratio. Most candidates contain W and Re, whose low-temperature brittleness is widely concerned; thus, Pugh's ratio was listed individually to evaluate alloy ductility. Tungsten carbide (WC) and pure tungsten were added as benchmark references. Note that the referenced single-crystal W here exhibits better ductility than common polycrystalline tungsten. It has been reported in the literature that single-crystal tungsten can be stretched by approximately 20% [72]. All alloys were initialized with equiatomic ratios in single-objective optimization. Partial high-performance compositions that exceeded empirical limits underwent minor ratio

adjustment to meet the constraints of δ, ΔH_{mix}, and VEC.

Table 5 compares predicted and DFT-calculated B and κ_l, together with estimated Vickers hardness. The micro-Vickers hardness is labeled as estimated because it is empirically fitted from the shear modulus and Pugh's ratio [73]. The SQS structures of the six BCC alloys were found to be dynamically unstable. Thereby, the Monte Carlo (MC) method was used to identify low-energy chemical short-range order (CSRO) stable configurations [19]. Subsequent mechanical and QHA phonon thermal transport calculations were conducted on these stable structures. The κ_l calculation, combining QHA and the Slack model, follows the standard AFLOW framework. QHA cannot capture high-order anharmonic effects, which is its major limitation [74]. Since anharmonic effects in HEAs significantly influence lattice thermal transport at elevated temperatures (especially significant above 770 K [75–77]), we exclusively selected κ_l at 300 K. This makes the description by QHA reasonably acceptable [75,78] although the κ_l of HEAs obtained from the QHA may slightly overestimate the actual value due to residual anharmonic effects. Nevertheless, as our work focuses on the comparative analysis of relative thermal conductivity values, the systematic error introduced by the algorithm does not substantially affect the rationality of composition screening.

Taking into account alloy properties, phase stability, precious metal prices and availability, we selected FCC-1, BCC-3, and BCC-4 from Table 5 as representative systems for further experimental validation. In our experimental validation, three alloys are labeled as Pt-1, RE-3 and RE-4, respectively, for convenience. The prefix 'Pt' denotes alloys composed mainly of platinum-group metals (PGMs), whereas 'RE' denotes refractory-metal-based alloys. The suffix numbers correspond to the sequence of isostructural alloys in Table 5. A detailed analysis is provided in the Discussion section below.

Figure 5a shows the XRD patterns. The Pt-1 alloy exhibits a dominant FCC (111) diffraction peak near 41°, accompanied by a minor precipitation of $Pt_{0.4}Re_{0.6}$ intermetallic HCP phase. RE-3 exhibits exceptional solid-solution behavior, showing only a single-phase BCC structure. For the RE-4 alloy, besides the dominant BCC main peaks, weak

diffraction signals from a precipitated Zr (HCP) and a $Re_{0.35}W_{0.65}$ intermetallic compound were also detected. Experimental lattice constants of the dominant phases match theoretical predictions remarkably well ((relative deviations below 0.7% for all samples in Table 6), and the phase structures of as-synthesized alloys are highly consistent with theoretical predictions.

Figure 5b–d shows the SEM surface morphologies and corresponding EDS elemental mappings of the three alloys. As shown by EDS mappings in Figs. 5b–d, microsegregation is evident in all the samples. Specifically, Pd segregates at grain boundaries of Pt-1, while distinct Zr precipitation occurs at grain boundaries of RE-3, and both Zr and Nb exhibit grain boundary segregation in RE-4.

Figure 5e presents the load–indentation depth curves for micro-Vickers hardness. Indentations were performed within the grain interiors, far from segregation zones, to eliminate the influence of the segregated phases. Under identical loads, RE-3 exhibits the largest indentation depth(lowest hardness), while Pt-1 shows the smallest depth (highest hardness). Typical indentation morphologies of three alloys are displayed in Figure 5f–h. The average microhardness and thermal conductivity data are summarized in Table 7. Small-punch testing of the as-cast alloys revealed a clear difference in room-temperature ductility (Figure 5i; Methods). Pt-1 reached a fracture deflection of 1.61 mm and a fracture energy of 529 mJ, corresponding to an equivalent tensile strength of approximately 500 MPa and an equivalent elongation of ~20% [79]. RE-4 showed an equivalent elongation below 10%, whereas RE-3 failed in a fully brittle manner.

Validation across alloy families and within-system composition variations

We tested whether the models reproduce property changes when a particular element is added to or removed from a fixed alloy system (Figs. 6a-d). (i) In the refractory Hf–Mo–Nb–Ta–Ti–Zr system, the presence of Mo, Ta or Zr increases the predicted *B* by 10.6%, 34.0% and 7.9%, respectively, relative to the corresponding element-free compositions. These responses are directionally consistent with the reported yield-strength changes (62.8%, 11.9% and 10.5%) [80], although *B* and yield strength are not directly

interchangeable. (ii) In AlxCoCrFeNi ($0 \leqslant x \leqslant 2$), the FCC and BCC contributions were weighted by the reported phase fractions. The predicted κ_l increases from 6.5 to 18.6 $W \cdot m^{-1} \cdot K^{-1}$ with rising Al content, reproducing the experimentally observed increase and subsequent saturation [81]. (iii) For three lightweight Al–Be–Mg–Ti–X (X = Li, Si, Cu) systems, compositions were modeled according to the literature-reported composition grids. The predicted B/ρ increases mildly with Be content and tracks the reported E/ρ trends, with the Si-bearing system being the stiffest in both prediction and experiment [82]. (iv) In $VCrFeTa_xW_x$, increasing the combined Ta + W content from x = 0.1 to x = 0.4 raises the predicted B from 148.1 $\pm$ 8.3 to 176.3 $\pm$ 9.4 GPa, consistent with the experimentally observed hardening trend [83].

To assess whether broad elemental coverage is accompanied by reliable predictions across known HEA classes, we next benchmarked the pre-trained models against 6 representative alloy families with independent experimental references: 3*d* transition-metal HEAs, Al-bearing and Cu-bearing 3*d* transition-metal HEAs, Mg alloys, refractory alloys, and refractory-alloy/TiC composites (in Figs. 6e, f and Supplementary Data). Random solid-solution models were constructed on the literature-reported phases; mixed-phase alloys were evaluated as the average of the constituent phases, and TiC-containing composites were modeled with TiC explicitly embedded in the alloy matrix. As shown in Fig. 6, the predicted B reproduces the experimental family-level ordering across all 6 families. The predicted κ_l reproduces the ordering for all families except Mg alloys, whose total thermal conductivity is dominated by the electronic contribution and therefore falls outside the lattice description. Together, these results demonstrate that the model's broad elemental coverage is supported by testable predictive consistency across diverse, established HEA families, rather than being limited to the compositions selected for optimization.

Discussion

The point worth noting is the variation in model performance across the partitioned subspaces. Although more detailed data-level evidence is currently lacking, the element-

type distributions in Figs. S1c and S2c suggest that the ternary and quaternary subspaces provide useful physical information while also introducing interference, and these two contributions are difficult to decouple.

With B and κ_l as dual optimization objectives, the optimized quinary FCC alloys converge to alloys containing W, Re, or both, combined with PGMs, whereas the BCC alloys are dominated by alloys containing W, Re, or both, combined with refractory metals, with Ti present in some cases (Fig. 4a). These results are consistent with metallurgical experience. W–Re alloys frequently exhibit excellent hardness [84], high-temperature strength and ductility [85] in refractory alloy researches [86], resulting in widely being used as structural materials in nuclear reactors [87,88] and wear-resistant materials [89]. Recent data-driven HEA research also reported the dominant role of W and Re in high-modulus refractory systems [66]. In addition, W and its alloys exhibit excellent thermal performance [90,91], with lattice thermal conductivity accounting for a significant proportion (33%) in W, reaching up to 46 $W \cdot m^{-1} \cdot K^{-1}$ [86]. Therefore, the preferential selection of W–Re systems reflects intrinsic physical properties rather than a data coincidence.

Examining the marginal distributions in Fig. 4a. Mo significantly enhances B: all refractory alloys with B >270 GPa contain Mo. Ti has a milder effect, yielding B of 250–265 GPa. These relative contributions agree with prior studies [80]. Previous refractory alloy studies show that Mo addition boosts strength but reduces toughness, while Ti delivers a better balance, consistent with the optimization results [92]. For κ_l, the top high-performance alloy possesses a total Ta and Nb content of over 90% (*at.*%). Ta and Nb have the same atomic radius of 1.46 Å, stable room temperature (RT) BCC structure [93], and highly comparable physicochemical properties; the two elements also frequently coexist in natural minerals [94]. The high similarity between Ta and Nb greatly reduces lattice distortion, which fundamentally accounts for its superior κ_l. Overall, the multi-objective optimization BCC results are fully consistent with fundamental metallurgical principles and physical expectations.

On the other hand, in Fig. 4b, the design of W–Re FCC quinary alloys with PGM additions has been rarely reported. Limited studies indicate that osmium (Os), as a W transmutation product, can strengthen W–Re alloys under irradiation conditions [87]. Iridium (Ir) within the PGMs improves the ductility of W–Re alloys while maintaining structural strength [95]. Consistent with these element-specific roles, the marginal distributions in Fig. 4b show that alloys with high Os content deliver a high *B* exceeding 255 GPa, while Ir-rich alloys exhibit moderate values ranging from 245 to 255 GPa. In this work, PGMs supply extra *d*-electrons, driving W–Re systems to form stable FCC structures instead of BCC. FCC alloys generally exhibit better RT ductility than BCC [96], which is consistent with their Pugh's ratios being higher than that of WC and close to that of single-crystal W (in Tables 4 and 5, data from MP database [56]). This trend was also reflected in room-temperature small-punch tests (SPTs), indicating that these FCC W–Re HEAs may be more ductile. Although the prohibitive cost of PGMs limits their conventional structural use, these AI-searched compositions expose a blind spot in traditional empirical design and could potentially be viable for precision devices, such as thermocouple wire.

DFT calculations were conducted to validate 11 single-objective bulk modulus alloys and 12 multi-objective optimized alloys, as listed in Tables 4 and 5. This validation aims to evaluate model accuracy and provide candidate alloys for subsequent experimental validation. Alloy performance, phase stability and raw material availability were comprehensively considered. All predicted data were calibrated via the linear fitting relationship in Fig. 3.

In Table 4, the maximum hardness of the searched alloys reached 1923.45 HV,

significantly higher than that of W single crystal. Its Pugh's ratio was close to W single crystal, reaching 1.85. Some scholars believe that when the Pugh's ratio exceeds 1.75, the material exhibits plasticity [97]. PGMs such as Pt and palladium (Pd) evidently act as bonding agents for the metals, while harder PGMs including ruthenium (Ru) and Os contribute to the enhancement of alloy hardness. Alloys with high B generally exhibit relatively high hardness, proving the rationality of taking B as the core optimization index.

As shown in Table 5, the lattice distortion of HEAs causes abundant phonon scattering, significantly reducing the κ_l of alloys. Compared with the quinary FCC alloys, BCC HEAs show notably higher κ_l, which is attributed to the larger average interatomic distance in the BCC phase. The increased open space allows for longer phonon mean free paths and higher phonon velocities [81]. On the other hand, the higher atomic mass in PGMs may also be the reason for their lower κ_l.

As shown in Fig. 5a and Table 6, the primary phases and lattice constants of three target alloys match theoretical predictions, verifying the feasibility of solid-solution alloy screening according to δ, ΔH_{mix} and VEC parameters, with all alloys possessing grain size of ~20 μm and distinct grain boundaries. Pt-1 contains minor HCP-structured $Pt_{0.4}Re_{0.6}$ intermetallic phase and Pd grain boundary segregation, which notably deteriorate its thermal conductivity and ductility; although increasing Pt and Pd contents can suppress such precipitation, it will increase material expenses. RE-3 achieves favorable solid solution from XRD results, yet Zr oxide precipitates occur at grain boundaries (Fig. 5c), resulting in a decrease in thermal conductivity to about 38% of the theoretical value, much lower than the other two alloys. For RE-4, $Re_{0.35}W_{0.65}$ intermetallic compound and slight undissolved Zr are detected, and the Zr segregation at grain boundaries observed by EDS is consistent with XRD results.

Table 7 summarizes the measured and calculated micro-Vickers hardness and thermal conductivity of the three target alloys. For the experimental values, Pt-1 exhibits the highest hardness of 816 ± 49 HV, followed by RE-4 (801 ± 9 HV), while RE-3

possesses the lowest value of 567 ± 7 HV. The hardness trend is highly consistent with theoretical predictions, with measured values accounting for 60–80% of calculated results.

The theoretical thermal conductivity in Table 7 is the sum of lattice thermal conductivity from Table 5 and electronic thermal conductivity calculated via the Kubo–Greenwood method [98] (see Section S7.1 for calculation details). The thermal conductivity trend is also consistent with theoretical predictions. The measured values for RE-4 and Pt-1 reach 60 – 65% of the theoretical predictions, whereas RE-3 shows markedly reduced thermal conductivity due to Zr oxide scattering. Among all samples, RE-4 exhibits the highest thermal conductivity. The thermal conductivity of Pt-1 is merely 8.583 ± 0.009 $W \cdot m^{-1} \cdot K^{-1}$. The ranking of thermal conductivity originates from the differences in structure (BCC or FCC) and atomic mass reflected in the Slack model.

Limited by experimental measurement, we could only obtain macroscopic thermal conductivity instead of microscale thermal transport. Defects including SRO, grain boundaries, precipitates and vacancies degrade thermal conductivity, making experimental values much lower than the theoretical value of single-phase solid solutions. Although micro-Vickers hardness was measured away from grain boundaries and segregation zones to eliminate the influence of segregated phases (Figs. 5f-h), the aforementioned defects still influence the hardness of the samples. In any case, our experimental data define a lower bound on the performance of the as-cast alloy with given compositions; we believe that optimized process of melting and heat treatment will push the properties of experiments toward the theoretical values. In addition to hardness and thermal conductivity testing, the SPT contrast between Pt-1 and the BCC alloys supports the design conjecture that PGM additions stabilize a more ductile FCC solid solution in intrinsically brittle W–Re systems. Although the empirical SPT conversion carries an uncertainty of ±20–30%, the difference between Pt-1 and RE-4 is sufficiently large to indicate a qualitative ductility advantage (in Fig. 5i). Conventional tensile tests and fracture-surface characterization will be required to establish this effect quantitatively.

Figure 6 evaluates whether the transferred models preserve known trends beyond the optimized candidates. At the family level, we investigated the experimental values of hardness and thermal conductivity for the six alloy families in the literature, and refractory HEAs combine high hardness with moderate-to-high thermal conductivity [99–101]. Mg alloys show high thermal conductivity [102,103], yet lowest hardness [102,104–106]. 3d transition-metal HEAs show low-to-intermediate values for hardness [107–110], and thermal conductivity [78,81,107,111]. Al-containing [81,112,113], Cu-containing [114] and TiC systems [115] shift these limits in the expected directions. The within-system tests capture the responses to element addition or removal (Figs. 6a-d), while the model predictions reproduce this alloy-family-level ordering (Figs. 6e and 6f). These results support the use of the framework for relative screening across alloy families and composition variations. Pt-1 and RE-4 lie within the refractory-alloy region, consistent with the optimization outcome.

All the above results indicate that HEAs with high hardness and lattice thermal conductivity are dominated by refractory-metal-rich compositions, which is consistent with the Pearson feature importance analysis in Figs. 2d and 2e. As shown in Figs. 2d and 2e, the element-weighted melting and boiling points make a markedly positive contribution to predicting both B and κ_l. Since melting and boiling points reflect the energy required to break interatomic bonds, bonding strength acts as the fundamental driving factor of a high melting point, and thus the core factor of enhancing both of the properties. Conventional understanding holds that the high strength [116] and hardness [117] of HEAs stem from solid-solution strengthening, which is a direct effect of lattice distortion [118]. Nevertheless, lattice distortion enhances phonon scattering, and reduces κ_l [119], resulting in a trade-off between hardness and thermal conductivity. In HEAs, bonding strength and lattice distortion function oppositely and restrict each other. It is essential to distinguish their independent contributions and coupling mechanisms in regulating

hardness and lattice thermal conductivity. Therefore, we chose W–Mo–Nb refractory ternary system as an example to clarify its composition–property relationship and internal physical origins.

Six ternary composition-property maps are presented in Fig. 7, with detailed calculation methods provided in Section S7.2 of the SI. In the W-Mo-Nb system, the weighted melting point and Integrated Crystal Orbital Hamilton Population (ICOHP) distributions are highly consistent and both reach their maxima near the W corner (in Figs. 7a and 7b), confirming that the weighted melting point is an efficient proxy for bonding strength. Lattice distortion is strongest near the Nb corner (Fig. 7c), whereas the equilibrium lattice constant also increases toward Nb (Fig. 7d). If lattice distortion alone governed the properties, the maximum B and minimum κ_l would occur near the center of the ternary map. Instead, strong W-Mo bonding shifts the maxima toward the W-Mo axis (Fig. 7e), meanwhile the smaller lattice constants near W and Mo increase bond density and shift the maximum B toward Mo. The smaller lattice constant also limits phonon anharmonicity, leading to higher κ_l along the Mo-Nb axis than along the W-Nb axis (Fig. 7f). Bonding strength, bond density and lattice distortion therefore jointly determine the composition-property landscape.

This work proposes a clear design principle for balanced mechanical and thermal transport properties of HEAs: preferentially selecting elements with high melting points and low equilibrium lattice constants, which explains why typical low-lattice-constant refractory elements such as W, Re and Mo occupy a dominant position in multi-objective optimization.

More broadly, this work demonstrates that universal materials databases can provide reliable property predictors for compositionally complex HEAs when their applicable domains are explicitly identified. Unlike many AI-assisted HEA studies that rely on newly compiled alloy-specific datasets, the present workflow combines Mix-GNN, TSPPES, independent pre-testing and linear calibration to screen compositions across nearly all non-radioactive metallic elements. The composition search required little training and search computing power. The effectiveness of the workflow therefore arises

from the complementarity between source-domain accuracy and target-space selection, and the same strategy should be applicable to other data-scarce material families when independent pre-testing data are available.

The present framework still focuses on ideal single-phase solid solutions and does not explicitly model precipitates, grain boundaries, dislocations or other multiscale defects, which can strongly affect real alloy performance. Future work should incorporate data and models for nanoscale short-range order [120,121], vacancies [15], defect structures [122], and grain boundaries [123], together with uncertainty quantification and feature-space distance metrics, to improve the generalizability of universal-database models to defective engineering alloys.

Methods

Model architecture, training and evaluation

A joint framework integrating GNN and MLP architectures, termed Mix-GNN, was employed for property prediction in this work. Mix-GNN is an invariant model in which the GNN component learns structural representations from crystal graphs, while the MLP component incorporates composition-, structure- and element-property-based features that are difficult for graph convolutions to extract. This combination is particularly useful for higher-order properties such as elastic constants and lattice thermal conductivity, for which purely graph-based representations may be insufficient.

The GNN branch uses the crystal graph convolutional neural network (CGCNN). Its main crystal graph convolutional layer is :

$$\boldsymbol{v}_i^{(t+1)}=\boldsymbol{v}_i^{(t)}+\sum_{j,k}\sigma\left(\boldsymbol{z}_{(i,j)k}^{(t)}W_f^{(t)}+b_f^{(t)}\right)\odot g\left(\boldsymbol{z}_{(i,j)k}^{(t)}W_s^{(t)}+b_s^{(t)}\right) \quad (1)$$

where σ, g and $\odot$ denote a sigmoid function, an activation function for introducing nonlinear coupling between layers and element-wise multiplication (Hadamard product), respectively. $W_f^{(t)}$, $W_s^{(t)}$, $b_f^{(t)}$ and $b_s^{(t)}$ are the convolution weight matrices, self-weight matrix, and bias of the t-th layer, respectively.

$\boldsymbol{z}_{(i,j)k}^{(t)}=\boldsymbol{v}_i^{(t)}\oplus\boldsymbol{v}_j^{(t)}\oplus\boldsymbol{u}_{(i,j)k}$ is the concatenation of atomic features with neighbor atomic features and edge features. $\boldsymbol{v}_i^{(t)}$ is the residual added to facilitate training in deeper networks.

For the MLP branch, 30 initial crystal features were extracted, covering elemental composition, crystal structure and weighted elemental properties. Discrete features were encoded through an embedding layer and concatenated with continuous features, followed by fully connected layers with residual connections. Feature selection was performed using Pearson correlation coefficients between the initial features and target properties, and features with absolute correlation coefficients above 0.02 were retained. In the mix layer, the CGCNN and MLP representations were combined through a Hadamard product and passed through a fully connected output layer.

Models were trained separately for bulk modulus and lattice thermal conductivity using log-transformed target values. Model performance on the universal validation sets was evaluated using the coefficient of determination,

$$R^2=1-\frac{\sum_{i=1}^{n}(Y_i-Y_i^{pre})^2}{\sum_{i=1}^{n}(Y_i-\bar{Y})^2} \tag{2}$$

where Y_i and Y_i^{pre} are the observed and predicted values, respectively, and $\bar{Y}$ is the mean observed value. For partitioned HEA subspaces, linear consistency was evaluated using the squared Pearson correlation coefficient,

$$r=\frac{\sum_{i=1}^{n}(Y_i-\bar{Y})\left(Y_i^{pre}-\overline{Y_{pre}}\right)}{\sqrt{\sum_{i=1}^{n}(Y_i-\bar{Y})^2\sum_{i=1}^{n}\left(Y_i^{pre}-\overline{Y_{pre}}\right)^2}} \tag{3}$$

R^2 was used to evaluate the fitting accuracy of a single model, whereas r^2 was used to assess whether predicted and reference values follow a consistent linear trend within each partitioned subspace. Because r^2 is bounded between 0 and 1 and remains meaningful in noisy subspaces where R^2 may become strongly negative, it was used to identify reliable regions for subsequent composition optimization.

Pre-testing datasets and target-space partitioning

A core step of TSPPES is to construct a reliable independent pre-testing set for evaluating model performance across material subspaces. Independent pre-testing datasets were constructed from published experimental and computational studies, comprising 178 bulk-modulus entries and 73 lattice-thermal-conductivity entries. The entries were classified by principal-element count and phase structure. Solid-solution structures were reproduced from the reported compositions and lattice parameters where available; otherwise, structures were generated using the procedure described in Supplementary Section 3. Linear relations between predicted and reported values were fitted within each validated subspace and used to calibrate subsequent predictions. The complete entries, references and calibration relations are listed in Supplementary Tables S2 and S3 and supplementary alloy structure data.

Candidate element selection and composition optimization

Unlimited screening of all metallic combinations is computationally costly and may yield chemically unstable solid solutions. Candidate elements were therefore selected using the Hume-Rothery rules [124] and the multi-component solid-solution phase-formation rules [125], while toxic, highly reactive and radioactive elements were excluded. For an *n*-component alloy with atomic fraction c_i and atomic radius r_i, the atomic-size mismatch is defined as:

$$\delta=\sqrt{\sum_{i=1}^{N} c_i(1-r_i/\bar{r})^2} \tag{4}$$

The mixing enthalpy is calculated as:

$$\Delta H_{mix}=\sum_{i=1,\, i\neq j}^{n} \Omega_{ij} c_i c_j \tag{5}$$

where Ω_{ij} ($=\Delta H_{AB}^{mix}$) is the regular melt-interaction parameter between *i*-th and *j*-th

elements, and ΔH_{AB}^{mix} is the mixing enthalpy of binary liquid alloys; the values can be obtained in reference [126]. The valence electron concentration (*VEC*) is an effective criterion for predicting alloy phase stability [127]. *VEC* is:

$$VEC=\sum_{i=1}^{n} c_i VEC_i \tag{6}$$

Stable solid solutions are generally expected when δ<0.045 and −22 kJ/mol < ΔH_{mix}< 5 kJ/mol [125]. When *VEC* > 8.0, FCC phases tend to form, whereas when *VEC* < 6.8, BCC phases tend to form [127].

Based on these rules, Fe, Zr, Cu, Mg and Ti were selected as central elements because of their widespread use in HEA research. According to Hume-Rothery rules, candidate elements were restricted to those with an atomic-radius mismatch of no more than 15% relative to the central elements. Toxic elements (Pb, Cd, Hg and In), highly reactive alkali metals (Na, K, Rb and Cs), and radioactive elements were excluded. The screened elements were then divided into 20 candidate subgroups according to the central element and further classified into normal, noble-metal-containing, rare-earth-containing and mixed groups, so that the effects of raw-material cost and element category could be examined separately. The complete element subgroups are listed in Table 3. Only all-metallic HEAs were considered; C, B, N, Si and P dopants were excluded because their interstitial occupancy and metal-nonmetal interactions introduce additional modeling complexity and can severely reduce plasticity [128].

Only single-phase solid-solution medium- and high-entropy alloys were evaluated. For each candidate composition, an FCC, BCC or HCP configuration was constructed using the special quasi-random structure (SQS) method. Lattice parameters were estimated from correlations among atomic radius, atomic mass and lattice constants fitted from the pre-testing datasets of the corresponding subspace.

Single-objective optimization of B and κ_l was used only to map the accessible ranges of the individual properties; these results and the corresponding tree-structured Parzen estimator (TPE) implementation are provided in Supplementary Information Section S6. Multi-objective optimization of B and κ_l was performed using NSGA-II [129]:

$$\begin{cases} \max B=f_B(E,p_i, S) \\ \max \kappa_l=f_{\kappa_l}(E,p_i, S) \end{cases}, \quad \text{subject to } \sum p_i=1,\ i=1, 2, \ldots, n \quad p_i\in[0.05,0.25],\ i=1, 2, \ldots, n \tag{7}$$

where f_B and f_{κ_l} denote the pre-trained property-prediction models, E is the elemental combination, p_i is the atomic fraction of the i-th element, and S denotes the crystal structure. For NSGA-II, the discrete elemental-combination variable was mapped to a continuous representation to support crossover and mutation, and the optimized value was mapped back to the original discrete combination for structure reconstruction.

After property prediction and composition optimization, candidates were pre-screened using δ, ΔH_{mix} and VEC. The final alloys were selected by additionally considering predicted performance, raw-material cost and phase-diagram information. These empirical restrictions were relaxed when necessary to avoid excluding potentially superior candidates during automated screening.

First-principles calculations

High-performance HEA candidates optimized by AI and pre-screened by empirical rules were validated through DFT calculations. Property evaluation under ideal lattice includes three core steps: structural optimization, mechanical calculation and lattice thermal transport calculation.

Structural optimization: **S**tructural optimization of pre-screened HEAs was carried out using VASP. For the DFT calculations, we utilized projector augmented wave (PAW) potentials [130] and the Perdew–Burke–Ernzerhof (PBE) [131] gradient approximation for the exchange-correlation functional. Brillouin zone integration was conducted using Gamma centered k-point meshes [132], with a k-point density of 4×4×4. The convergence criteria for ionic relaxation and electronic self-convergence were set at 1.0×10^{-2} eV·Å^{-1} and 1.0×10^{-5} eV·atom^{-1}, respectively. The plane-wave energy cutoff was fixed at 550 eV.

Mechanical calculation: Elastic constants C_{ij} are defined by the second derivative of total energy with respect to external strain [71]. The key mechanical properties of the target HEA, including B, shear modulus (G), Young's modulus (Y), micro-Vickers hardness (H_V) [73], Poisson's ratio (σ), and Pugh's ratio ($k=B/G$) [97] can be derived from elastic constants. Taking cubic crystal systems as an example:

$$B_V=B_R=B_H=\frac{1}{3}(C_{11}+2C_{12}) \tag{8}$$

$$G_V=\frac{1}{5}[(C_{11}-C_{12})+3C_{44}] \tag{9}$$

$$G_R=\frac{5C_{44}(C_{11}-C_{12})}{3(C_{11}-C_{12})+4C_{44}} \tag{10}$$

$$G_H=\frac{1}{2}(G_V+G_R) \tag{11}$$

$$Y=\frac{9B_HG_H}{3B_H+G_H} \tag{12}$$

$$H_V=2(k^{-2}G)^{0.585}-3 \tag{13}$$

$$\sigma=\frac{3B_H-2G_H}{2(3B_H+G_H)} \tag{14}$$

where subscripts V, R, and H are denoted as Voigt, Reuss, and Hill approximations, respectively. All mechanical property calculations can be completed by VASP and VASPKIT [133].

Lattice thermal conductivity calculation: The QHA method was used for calculation, with reference to the literature [59]. The calculated κ_l of HEAs using this method may lack absolute accuracy. Nevertheless, it is adequate for comparing relative property values in this work.

According to the theory proposed by Slack [70], the thermal conductivity contributed by lattice vibration is expressed as follows:

$$\kappa_l=A\frac{\bar{M}\theta_D^3\delta}{\gamma^2n^{2/3}T} \tag{15}$$

where n is the number of atoms in the supercell, δ is the cube root of volume per atom, $\bar{M}$ is the average atomic mass, and the constant A is 3.1×10^{-6} when the unit of the thermal conductivity is $W\cdot m^{-1}\cdot K^{-1}$ and δ is taken as Å, respectively. T is

temperature, and γ is Grüneisen parameter, which can be calculated by Phonopy [68,134,135]. The Debye temperature θ_D is calculated by the following formula [136]:

$$\theta_D = \frac{\hbar}{k_B}(6\pi^2 V^{1/2} n)^{1/3} f(\sigma)\sqrt{\frac{B}{\overline{M}}} \tag{16}$$

Here, $f(\sigma)$ relates to Poisson's ratio (σ) [137], being:

$$f(\sigma) = \left\{3\left[2\left(\frac{2}{3}\frac{1+\sigma}{1-2\sigma}\right)^{3/2} + \left(\frac{1}{3}\frac{1+\sigma}{1-\sigma}\right)^{3/2}\right]^{-1}\right\}^{1/3} \tag{17}$$

Experimental Methods

Alloy preparation: The alloy ingots were prepared by vacuum arc-melting in a water-cooled copper mold in a Ti-gettered high-purity argon atmosphere. The purity of the constituent elements was higher than 99.9 *wt*.%, and the elements were pre-cut into uniform 2×2×2 mm^3 particles. Since the alloy systems involved are all refractory alloys, each ingot was flipped and remelted 12 times during melting to improve chemical homogeneity. Before melting, burn-off tests were carried out; to compensate for Pd loss during melting, an extra 21.23 *wt.*% of Pd was added relative to the designed composition. The as-cast alloy ingots were cut and polished for structural characterization and measurements of their thermal transport and mechanical properties.

Sample characterization and property measurement: The morphology and elemental distribution of the polished ingots were examined using a scanning electron microscope (SEM, GAIA3 TESCAN) equipped with an energy-dispersive X-ray spectrometer (EDS). The phase constitution was characterized by X-ray diffraction and grazing incidence X-ray diffraction (XRD and GIXRD; DX-2700BH, HAOYUAN, China) using Cu Kα radiation (λ = 0.154 nm). Scans were performed over a 2θ range of 30–90° with a step size of 0.01° and a dwell time of 1 s. Micro Vickers hardness of the alloys was tested by a nanoscale mechanical tester (KLA G200X) under a load of 245 mN for 19 s loading time in continuous stiffness measurement (CSM) mode. Twelve indentations at different regions were conducted for each specimen, and their average value at non-grain boundaries was calculated as the test result to fit the theoretical

calculation conditions. The total thermal conductivity (κ_t, all measurements and discussions in the experimental section refer to the total thermal conductivity.) of the test material can be calculated by [138,139]:

$$\kappa_t=\alpha\rho C_p \quad (18)$$

where, α is the thermal diffusion coefficient; ρ is the density; and C_p is the specific heat capacity. A light flash system (Netzsch LFA 467) was used to measure the thermal diffusion coefficient of the specimens (Φ 10 mm×2 mm) at RT. The specific heat capacity of the alloy was calculated by the Neumann-Kopp's rule [140]. The density of specimens at RT was determined based on the Archimedes' principle.

An SPT tester (Model OTF-1500X-S-CR, Hefei Kejing Materials Technology Co., Ltd., China) was used to test the sample at RT. The descent speed of the indenter was set to 1.0 mm/min, and the sample thickness is 0.5mm. The load-displacement curve was recorded during the test, and the equivalent tensile strength and elongation were calculated based on the curve and the conversion formula. [79].

Code availability

All code used in this work is available on GitHub at https://github.com/xiezhen087/HEA-LTC-BM. The manual branch preserves the original human-developed core code, mainly including model architecture, training and inference, data processing, and feature engineering, while the main branch contains the complete project, including additional AI-assisted code mainly for data visualization and project packaging.

Data Availability

Source data for Tables 4-7 and all data-generated figures, including the experimental and literature-validation data, are available on Zenodo at https://doi.org/10.5281/zenodo.23938398. The MP and AFLOW IDs used for model training/validation and alloy structures in pre-testing datasets are provided with the code on GitHub at https://github.com/xiezhen087/HEA-LTC-BM. Modeling and property details for all pre-testing alloys are provided in the Supplementary Information.

Received: ((will be filled in by the editorial staff)); Accepted: ((will be filled in by the editorial staff)); Published online: ((will be filled in by the editorial staff))

References

1. Butler, K. T., Davies, D. W., Cartwright, H., Isayev, O. & Walsh, A. Machine learning for molecular and materials science. *Nature* **559**, 547–555 (2018).

2. Hart, G. L. W., Mueller, T., Toher, C. & Curtarolo, S. Machine learning for alloys. *Nat. Rev. Mater.* **6**, 730–755 (2021).

3. Reiser, P. *et al.* Graph neural networks for materials science and chemistry. *Commun. Mater.* **3**, 93 (2022).

4. Wang, S. *et al.* Artificial Intelligence Empowers Solid-State Batteries for Material Screening and Performance Evaluation. *Nano-Micro Lett.* **17**, 287 (2025).

5. Ma, J. *et al.* MLMD: a programming-free AI platform to predict and design materials. *Npj Comput. Mater.* **10**, 59 (2024).

6. Li, Z. *et al.* APEX: an automated cloud-native material property explorer. *Npj Comput. Mater.* **11**, 88 (2025).

7. Yang, H. *et al.* MatterSim: A Deep Learning Atomistic Model Across Elements, Temperatures and Pressures. Preprint at https://doi.org/10.48550/arXiv.2405.04967 (2024).

8. Zhichao, L., Dong, M., Xiongjun, L. & Lu, Z. High-throughput and data-driven machine learning techniques for discovering high-entropy alloys. *Commun. Mater.* **5**, 76 (2024).

9. Liu, P. *et al.* Machine learning assisted design of γ′-strengthened Co-base superalloys with multi-performance optimization. *Npj Comput. Mater.* **6**, 62 (2020).

10. Peng, J., Yamamoto, Y., Hawk, J. A., Lara-Curzio, E. & Shin, D. Coupling physics in machine learning to predict properties of high-temperatures alloys. *Npj Comput. Mater.* **6**, 141 (2020).

11. Cheng, G., Gong, X.-G. & Yin, W.-J. Crystal structure prediction by combining graph network and optimization algorithm. *Nat. Commun.* **13**, 1492 (2022).

12. Merchant, A. *et al.* Scaling deep learning for materials discovery. *Nature* **624**, 80–85 (2023).

13. Zeni, C. *et al.* A generative model for inorganic materials design. *Nature* **639**, 624–632 (2025).

14. Fu, C. *et al.* AI-Driven Defect Engineering for Advanced Thermoelectric Materials. *Adv. Mater.* 2505642 (2025) doi:10.1002/adma.202505642.

15. Xing, B., Rupert, T. J., Pan, X. & Cao, P. Neural network kinetics for exploring diffusion multiplicity and chemical ordering in compositionally complex materials. *Nat. Commun.* **15**, 3879 (2024).

16. Li, Y. *et al.* Accelerating defect analysis of solar cells via machine learning of the modulated transient photovoltage. *Fundam. Res.* **4**, 1650–1656 (2024).

17. Zhong, X. *et al.* Explainable machine learning in materials science. *Npj Comput. Mater.* **8**, 204 (2022).

18. Jiang, X. *et al.* Interpretable Machine Learning Applications: A Promising Prospect of AI for Materials. *Adv. Funct. Mater.* 2507734 (2025) doi:10.1002/adfm.202507734.

19. Shi, P. *et al.* Exploration for the physical origin and impact of chemical short-range order in high-entropy alloys: Machine learning-assisted study. *Mater. Des.* **253**, 113892 (2025).

20. Elkatatny, S., Abd-Elaziem, W., Sebaey, T. A., Darwish, M. A. & Hamada, A. Machine-learning synergy in high-entropy alloys: A review. *J. Mater. Res. Technol.* **33**, 3976–3997 (2024).

21. Chaudhary, V., Chaudhary, R., Banerjee, R. & Ramanujan, R. V. Accelerated and conventional development of magnetic high entropy alloys. *Mater. Today* **49**, 231–252 (2021).

22. Liu, X., Zhang, J. & Pei, Z. Machine learning for high-entropy alloys: Progress, challenges and opportunities. *Prog. Mater. Sci.* **131**, 101018 (2023).

23. Yeh, J.-W. Recent progress in high-entropy alloys. *Ann. Chim. Sci. Matér.* **31**, 633–648 (2006).

24. Zou, C. *et al.* Integrating data mining and machine learning to discover high-strength ductile titanium alloys. *Acta Mater.* **202**, 211–221 (2021).

25. Sohail, Y. *et al.* Machine-learning design of ductile FeNiCoAlTa alloys with high strength. *Nature* https://doi.org/10.1038/s41586-025-09160-2 (2025) doi:10.1038/s41586-025-09160-2.

26. Wen, C. *et al.* Machine learning assisted design of high entropy alloys with desired property. *Acta Mater.* **170**, 109–117 (2019).

27. Yang, C. *et al.* A machine learning-based alloy design system to facilitate the rational design of high entropy alloys with enhanced hardness. *Acta Mater.* **222**, 117431 (2022).

28. Roy, A. *et al.* Rapid discovery of high hardness multi-principal-element alloys using a generative adversarial network model. *Acta Mater.* **257**, 119177 (2023).

29. Ren, W., Zhang, Y.-F., Wang, W.-L., Ding, S.-J. & Li, N. Prediction and design of high hardness high entropy alloy through machine learning. *Mater. Des.* **235**, 112454 (2023).

30. Ma, Y., Li, M., Mu, Y., Wang, G. & Lu, W. Accelerated Design for High-Entropy Alloys Based on Machine Learning and Multiobjective Optimization. *J. Chem. Inf. Model.* **63**, 6029–6042 (2023).

31. Qian, J., Li, Y., Hou, J., Wu, S. & Zou, Y. Accelerating the development of Fe–Co–Ni–Cr system

HEAs with high hardness by deep learning based on Bayesian optimization. *J. Mater. Res.* **39**, 2115–2130 (2024).

32. Wang, Z. *et al.* Coupling high-throughput experiment and machine learning to optimize elemental composition in nickel-based superalloys. *MRS Commun.* **11**, 411–417 (2021).

33. Chen, C., Ma, L., Zhang, Y., Liaw, P. K. & Ren, J. Accelerating the design of high-entropy alloys with high hardness by machine learning based on particle swarm optimization. *Intermetallics* **154**, 107819 (2023).

34. Dey, D. *et al.* Developing new high-entropy alloys with enhanced hardness using a hybrid machine learning approach: integrating interpretability and NSGA-II optimization. *J. Mater. Sci.* **60**, 4820–4845 (2025).

35. Gao, J. *et al.* Machine learning assisted study of phase and properties in cobalt-free AlCrxCuFeNi2 high-entropy alloys. *J. Alloys Compd.* **1002**, 175541 (2024).

36. Vashistha, S., Mahanta, B. K., Singh, V. K. & Singh, S. K. Machine learning assisted optimization of tribological parameters of Al–Co–Cr–Fe–Ni high-entropy alloy. *Mater. Manuf. Process.* **38**, 2093–2106 (2023).

37. Yang, W. *et al.* Accelerated design of $L1_2$ -strengthened single crystal high entropy alloys based on machine learning and multi-objective optimization. *Mater. Adv.* **5**, 5772–5780 (2024).

38. Li, Y. *et al.* Developing novel low-density high-entropy superalloys with high strength and superior creep resistance guided by automated machine learning. *Acta Mater.* **285**, 120656 (2025).

39. Odetola, P. I. *et al.* Exploring high entropy alloys: A review on thermodynamic design and

computational modeling strategies for advanced materials applications. *Heliyon* **10**, e39660 (2024).

40. Rao, Z. *et al.* Machine learning–enabled high-entropy alloy discovery. *Science* **378**, 78–85 (2022).

41. Zhang, H. *et al.* Empowering the Sustainable Development of High-End Alloys via Interpretive Machine Learning. *Adv. Mater.* **36**, 2404478 (2024).

42. USDOE Office of Nuclear Energy (NE), Idaho National Laboratory (INL), Idaho Falls, ID (United States), Barrett, K., Bragg-Sitton, S. & Galicki, D. *Advanced LWR Nuclear Fuel Cladding System Development Trade-Off Study*. INL/EXT-12-27090, 1057698 https://www.osti.gov/biblio/1057698 (2012) doi:10.2172/1057698.

43. Wang, Y. *et al.* Evaluation of the thermal conductivity of chromium coatings for accident tolerant fuels using thermoreflectance techniques. *J. Nucl. Mater.* **604**, 155535 (2025).

44. Guo, T., Wu, L. & Li, T. Machine Learning Accelerated, High Throughput, Multi-Objective Optimization of Multiprincipal Element Alloys. *Small* **17**, 2102972 (2021).

45. Yu, A., Pan, Y., Wan, F., Kuang, F. & Lu, X. Multi-objective optimization of laser powder bed fused titanium considering strength and ductility: A new framework based on explainable stacking ensemble learning and NSGA-II. *J. Mater. Sci. Technol.* **228**, 241–255 (2025).

46. Wen, C. *et al.* Machine-Learning-Assisted Compositional Design of Refractory High-Entropy Alloys with Optimal Strength and Ductility. *Engineering* **46**, 214–223 (2025).

47. Zhang, Y. *et al.* Toward ultra-high strength high entropy alloys via feature engineering. *J. Mater. Sci. Technol.* **200**, 243–252 (2024).

48. Terrani, K. A. Accident tolerant fuel cladding development: Promise, status, and challenges. *J. Nucl. Mater.* **501**, 13–30 (2018).

49. Yu, J. *et al.* Unique Role of Refractory Ta Alloying in Enhancing the Figure of Merit of NbFeSb Thermoelectric Materials. *Adv. Energy Mater.* **8**, 1701313 (2018).

50. Ma, S. & Zhao, S. Tunable lattice thermal transport properties in high-entropy alloys through manipulating chemical short-range order guided by machine learning. *Mater. Des.* **255**, 114195 (2025).

51. Fan, Z., Wang, H., Wu, Y., Liu, X. J. & Lu, Z. P. Thermoelectric high-entropy alloys with low lattice thermal conductivity. *RSC Adv.* **6**, 52164–52170 (2016).

52. Kush, L., Srivastava, S., Jaiswal, Y. & Srivastava, Y. Thermoelectric behaviour with high lattice thermal conductivity of Nickel base $Ni_2CuCrFeAl_x$ (x = 0.5, 1.0, 1.5 and 2.5) high entropy alloys. *Mater. Res. Express* **7**, 035704 (2020).

53. Wang, H. *et al.* Exceptionally low thermal conductivity in distorted high entropy alloy. *Mater. Res. Lett.* **13**, 24–34 (2025).

54. Wen, C. *et al.* Accelerated discovery of refractory high-entropy alloys for strength-ductility co-optimization: An exploration in NbTaZrHfMo system by machine learning. *Scr. Mater.* **252**, 116240 (2024).

55. Han, B. *et al.* AI-powered exploration of molecular vibrations, phonons, and spectroscopy. *Digit. Discov.* **4**, 584–624 (2025).

56. Jain, A. *et al.* Commentary: The Materials Project: A materials genome approach to accelerating materials innovation. *APL Mater.* **1**, 011002 (2013).

57. Mehl, M. J. *et al.* The AFLOW Library of Crystallographic Prototypes: Part 1. *Comput. Mater. Sci.* **136**, S1–S828 (2017).

58. De Jong, M. *et al.* Charting the complete elastic properties of inorganic crystalline compounds. *Sci. Data* **2**, 150009 (2015).

59. Toher, C. *et al.* High-throughput computational screening of thermal conductivity, Debye temperature, and Grüneisen parameter using a quasiharmonic Debye model. *Phys. Rev. B* **90**, (2014).

60. Loew, A., Sun, D., Wang, H.-C., Botti, S. & Marques, M. A. L. Universal machine learning interatomic potentials are ready for phonons. *Npj Comput. Mater.* **11**, 178 (2025).

61. Zhang, R. *et al.* Core Electron Count as a Versatile and Accurate New Descriptor for Sorting Mechanical Properties of Diverse Transition Metal Compounds. *Adv. Mater.* **35**, (2023).

62. Liu, C. *et al.* General theory for designing phonon transport in alloyed/doped materials. *Sci. China Phys. Mech. Astron.* **67**, (2024).

63. Torsti, V., Mäkinen, T., Bonfanti, S., Koivisto, J. & Alava, M. J. Improving the mechanical properties of Cantor-like alloys with Bayesian optimization. *APL Mach. Learn.* **2**, 016119 (2024).

64. Li, M. *et al.* Composition driven machine learning for unearthing high-strength lightweight multi-principal element alloys. *J. Alloys Compd.* **1008**, 176517 (2024).

65. Das, P. & Pandey, P. M. Multi-objective optimization and machine learning assisted design and synthesis of magnesium based novel non-equiatomic medium entropy alloy. *J. Alloys Compd.* **985**, 174066 (2024).

66. Dai, M. *et al.* Data-Driven Design of Mechanically Hard Soft Magnetic High-Entropy Alloys. *Adv. Sci.* **12**, 2500867 (2025).

67. Kresse, G. & Furthmüller, J. Efficient iterative schemes for*ab initio*total-energy calculations using a plane-wave basis set. *Phys. Rev. B* **54**, 11169–11186 (1996).

68. Togo, A. & Tanaka, I. First principles phonon calculations in materials science. *Scr. Mater.* **108**, 1–5 (2015).

69. Boltzmann, L. Further Studies on the Thermal Equilibrium of Gas Molecules. in *History of Modern Physical Sciences* vol. 1 262–349 (PUBLISHED BY IMPERIAL COLLEGE PRESS AND DISTRIBUTED BY WORLD SCIENTIFIC PUBLISHING CO., 2003).

70. Slack, G. A. Nonmetallic crystals with high thermal conductivity. *J. Phys. Chem. Solids* **34**, 321–335 (1973).

71. Mouhat, F. & Coudert, F.-X. Necessary and sufficient elastic stability conditions in various crystal systems. *Phys. Rev. B* **90**, 224104 (2014).

72. Shi, J. *et al.* Experiments and/or crystal plasticity finite element modeling of the mechanical properties of pristine and irradiated tungsten single crystal. *Int. J. Plast.* **154**, 103293 (2022).

73. Chen, X.-Q., Niu, H., Li, D. & Li, Y. Modeling hardness of polycrystalline materials and bulk metallic glasses. *Intermetallics* **19**, 1275–1281 (2011).

74. Blancas, E. J. *et al.* Thermodynamics of solids including anharmonicity through quasiparticle theory. *Npj Comput. Mater.* **10**, 267 (2024).

75. Chen, H. *et al.* Realization of Fine-Tuning the Lattice Thermal Conductivity and Anharmonicity in Layered Semiconductors via Entropy Engineering. *Adv. Mater.* **36**, 2400911 (2024).

76. Uporov, S. A. *et al.* Unraveling thermal evolution and anisotropy in BCC TiVNbMo high entropy alloy via in situ XRD and first-principles simulations. *Intermetallics* **189**, 109092 (2026).

77. Bykov, V. A. *et al.* Transport Properties of Equiatomic CoCrFeNi High-Entropy Alloy with a Single-Phase Face-Centered Cubic Structure. *Crystals* **13**, 1567 (2023).

78. Yang, J. *et al.* Mictomagnetism and suppressed thermal conduction of the prototype high-entropy alloy CrMnFeCoNi. *J. Mater. Sci. Technol.* **99**, 55–60 (2022).

79. Frelek-Kozak, M. *et al.* Evaluation of consolidation method on mechanical and structural properties of ODS RAF steel. *Appl. Surf. Sci.* **446**, 215–221 (2018).

80. Tseng, K.-K. *et al.* Effects of Mo, Nb, Ta, Ti, and Zr on Mechanical Properties of Equiatomic Hf-Mo-Nb-Ta-Ti-Zr Alloys. *Entropy* **21**, 15 (2018).

81. Chou, H.-P., Chang, Y.-S., Chen, S.-K. & Yeh, J.-W. Microstructure, thermophysical and electrical properties in AlxCoCrFeNi (0≤x≤2) high-entropy alloys. *Mater. Sci. Eng. B* **163**, 184–189 (2009).

82. Sorkin, V. *et al.* First principles-based design of lightweight high entropy alloys. *Sci. Rep.* **13**, 22549 (2023).

83. Zhang, W., Liaw, P. K. & Zhang, Y. A Novel Low-Activation VCrFeTaxWx (x = 0.1, 0.2, 0.3, 0.4, and 1) High-Entropy Alloys with Excellent Heat-Softening Resistance. *Entropy* **20**, 951 (2018).

84. Jiang, D., Xiao, W., Liu, D. & Liu, S. Structural stability, electronic structures, mechanical properties and debye temperature of W-Re alloys: A first-principles study. *Fusion Eng. Des.* **162**,

112081 (2021).

85. Ivanov, E. Y., Suryanarayana, C. & Bryskin, B. D. Synthesis of a nanocrystalline W–25 wt.% Re alloy by mechanical alloying. *Mater. Sci. Eng. A* **251**, 255–261 (1998).

86. Zheng, Z. *et al.* Preparation, Mechanical Properties and Strengthening Mechanism of W-Re Alloys: A Review. *Materials* **17**, 102 (2023).

87. Tanno, T. *et al.* Effects of Transmutation Elements on Neutron Irradiation Hardening of Tungsten. *Mater. Trans.* **48**, 2399–2402 (2007).

88. Hasegawa, A., Fukuda, M., Nogami, S. & Yabuuchi, K. Neutron irradiation effects on tungsten materials. *Fusion Eng. Des.* **89**, 1568–1572 (2014).

89. Miles, M. P. *et al.* Impact of tool wear on joint strength in friction stir spot welding of DP 980 steel. *Sci. Technol. Weld. Join.* **16**, 642–647 (2011).

90. Yamamoto, T., Hara, M. & Hatano, Y. Cracking behavior and microstructural, mechanical and thermal characteristics of tungsten–rhenium binary alloys fabricated by laser powder bed fusion. *Int. J. Refract. Met. Hard Mater.* **100**, 105651 (2021).

91. Nogami, S. *et al.* Solid state diffusion bonding of doped tungsten alloys with different thermo-mechanical properties. *Fusion Eng. Des.* **136**, 76–81 (2018).

92. Sun, R. *et al.* Accelerated discovery through multi-property screening strategy: Achieving strength-ductility synergy in TiZrHfNbMoTa RHEAs. *Int. J. Refract. Met. Hard Mater.* **134**, 107412 (2026).

93. Sugi, C. *et al.* Site Change of Hydrogen Owing to Lattice Distortion in Niobium Alloys. *J. Phys. Soc. Jpn.* **82**, 074601 (2013).

94. Kuzmenko, M. V. THE GEOCHEMISTRY OF TANTALUM AND NIOBIUM. *Int. Geol. Rev.* **3**, 9–25 (1961).

95. Luo, A., Jacobson, D. L. & Shin, K. S. Solution softening mechanism of iridium and rhenium in tungsten at room temperature. *Int. J. Refract. Met. Hard Mater.* **10**, 107–114 (1991).

96. George, E. P., Curtin, W. A. & Tasan, C. C. High entropy alloys: A focused review of mechanical properties and deformation mechanisms. *Acta Mater.* **188**, 435–474 (2020).

97. Pugh, S. F. XCII. Relations between the elastic moduli and the plastic properties of polycrystalline pure metals. *Lond. Edinb. Dublin Philos. Mag. J. Sci.* **45**, 823–843 (1954).

98. Calderín, L., Karasiev, V. V. & Trickey, S. B. Kubo–Greenwood electrical conductivity formulation and implementation for projector augmented wave datasets. *Comput. Phys. Commun.* **221**, 118–142 (2017).

99. Shkodich, N. F. *et al.* Refractory TaTiNb, TaTiNbZr, and TaTiNbZrX (X = Mo, W) high entropy alloys by combined use of high energy ball milling and spark plasma sintering: Structural characterization, mechanical properties, electrical resistivity, and thermal conductivity. *J. Alloys Compd.* **893**, 162030 (2022).

100. Ryltsev R.E., Estemirova S. Kh., Yagodin D. A., Sterkhov E. V., & Uporov S. A. Structure, thermal stability and transport properties of heat-resistant high-entropy ZrTiHfNb alloy. *Phys. Solid State* **64**, 2266 (2022).

101. Li, Q. *et al.* Enhanced elasticity, fracture toughness and hardness in refractory TiZrHfNb high-entropy alloys by N- and O- doping engineering. *Intermetallics* **181**, 108714 (2025).

102. Liao, Q. *et al.* Effect of solid solution and precipitation on thermal conductivity and mechanical

properties of Mg–Zn–Cu–Ce magnesium alloy. *J. Mater. Res. Technol.* **35**, 5923–5932 (2025).

103. Xiang, C., Huang, Z., Wang, Z., Ding, H. & Xu, S. Effect of Cu addition on the microstructure, mechanical properties and thermal properties of Mg-Al-Ca-Mn alloy. *Mater. Charact.* **202**, 113028 (2023).

104. Liu, C. & Liu, Y. Effect of extrusion and annealing processes onmicrostructure and properties of Mg-Al-Ca-Mn-Cu-Ni soluble magnesium alloys. (Qilu University of Technology, 2021).

105. Liu, D., Xin, R., Zheng, X., Zhou, Z. & Liu, Q. Microstructure and mechanical properties of friction stir welded dissimilar Mg alloys of ZK60–AZ31. *Mater. Sci. Eng. A* **561**, 419–426 (2013).

106. Elamami, H. A., Incesu, A., Korgiopoulos, K., Pekguleryuz, M. & Gungor, A. Phase selection and mechanical properties of permanent-mold cast Mg-Al-Ca-Mn alloys and the role of Ca/Al ratio. *J. Alloys Compd.* **764**, 216–225 (2018).

107. Bag, P., Su, Y.-C., Kuo, Y.-K., Lai, Y.-C. & Wu, S.-K. Physical properties of face-centered cubic structured high-entropy alloys: Effects of NiCo, NiFe, and NiCoFe alloying with Mn, Cr, and Pd. *Phys. Rev. Mater.* **5**, 085003 (2021).

108. Wang, W.-R. *et al.* Effects of Al addition on the microstructure and mechanical property of AlxCoCrFeNi high-entropy alloys. *Intermetallics* **26**, 44–51 (2012).

109. Liu, S. *et al.* A comparative study on nanoscale mechanical properties of CrMnFeCoNi high-entropy alloys fabricated by casting and additive manufacturing. *J. Mater. Res. Technol.* **33**, 1211–1219 (2024).

110. Wu, J. & Gao, Y. Low temperature hardening and toughening of CoCrFeMnNi and HSLA laser-

welded joint by nano twin. *Opt. Laser Technol.* **198**, 114952 (2026).

111. Jin, K. *et al.* Tailoring the physical properties of Ni-based single-phase equiatomic alloys by modifying the chemical complexity. *Sci. Rep.* **6**, 20159 (2016).

112. Zhang, J. *et al.* Mechanical properties and water vapour corrosion behaviour of Al_x CoCrFeNi high-entropy alloys. *RSC Adv.* **14**, 24741–24748 (2024).

113. Ma, J. Research on Microstructure and Properties of Al_xCoCrFeNi High-Entropy Alloy. *Adv. Mater. Chem.* **09**, 66–70 (2021).

114. Rodríguez-López, A., Savoini, B., Monge, M. A., Galatanu, A. & Galatanu, M. Evaluation of thermal properties of CuCrFeV (Ti, Ta, W, Mo) for nuclear fusion applications. *Nucl. Mater. Energy* **41**, 101767 (2024).

115. Chang, C. *et al.* Thermal and Mechanical Properties of Refractory High-Entropy Alloy Composites with TiC in Nonequal Molar CrMoNbTaTiZr at Elevated Temperatures. *Adv. Eng. Mater.* **28**, e202502055 (2026).

116. Yeh, J. -W. *et al.* Nanostructured High-Entropy Alloys with Multiple Principal Elements: Novel Alloy Design Concepts and Outcomes. *Adv. Eng. Mater.* **6**, 299–303 (2004).

117. Chen, M.-R. *et al.* Microstructure and Properties of Al0.5CoCrCuFeNiTix (x=0-2.0) High-Entropy Alloys. *Mater. Trans.* **47**, 1395–1401 (2006).

118. Roy, A. *et al.* Lattice distortion as an estimator of solid solution strengthening in high-entropy alloys. *Mater. Charact.* **172**, 110877 (2021).

119. Nagarjuna, C. *et al.* Entropy engineering stimulates the thermoelectric performance of FeCoNiAlSix high-entropy alloys. *Mater. Res. Bull.* **188**, 113404 (2025).

120. Elsborg, J. & Bhowmik, A. ArtiSAN: navigating the complexity of material structures with deep reinforcement learning. *Mach. Learn. Sci. Technol.* **5**, 035043 (2024).

121. Li, C., Liang, H., Duan, Y. & Lin, Z. Machine-learning accelerated annealing with fitting-search style for multicomponent alloy structure predictions. *Phys. Rev. Mater.* **7**, 033802 (2023).

122. Na, G. S., Jang, S. & Chang, H. Predicting thermoelectric properties from chemical formula with explicitly identifying dopant effects. *Npj Comput. Mater.* **7**, 106 (2021).

123. Zheng, H. *et al.* Grain boundary properties of elemental metals. *Acta Mater.* **186**, 40–49 (2020).

124. Reed-Hill, R. E. & Abbaschian, R. *Physical Metallurgy Principles*. (PWS-Kent Pub, Boston, 1992).

125. Zhang, Y., Zhou, Y. J., Lin, J. P., Chen, G. L. & Liaw, P. K. Solid-Solution Phase Formation Rules for Multi-component Alloys. *Adv. Eng. Mater.* **10**, 534–538 (2008).

126. Takeuchi, A. & Inoue, A. Classification of Bulk Metallic Glasses by Atomic Size Difference, Heat of Mixing and Period of Constituent Elements and Its Application to Characterization of the Main Alloying Element. *Mater. Trans.* **46**, 2817–2829 (2005).

127. Guo, S., Ng, C., Lu, J. & Liu, C. T. Effect of valence electron concentration on stability of fcc or bcc phase in high entropy alloys. *J. Appl. Phys.* **109**, 103505 (2011).

128. Liu, Z., Guo, L., Yan, Z., Liu, T. & Fu, Q. Enhance mechanical properties and ablation resistance of high-entropy (Hf0.25Zr0.25Ti0.25Ta0.25)C ceramics by introducing W metal. *Ceram. Int.* **52**, 4017–4027 (2026).

129. Deb, K., Pratap, A., Agarwal, S. & Meyarivan, T. A fast and elitist multiobjective genetic algorithm: NSGA-II. *IEEE Trans. Evol. Comput.* **6**, 182–197 (2002).

130. Blöchl, P. E. Projector augmented-wave method. *Phys. Rev. B* **50**, 17953–17979 (1994).

131. Perdew, J. P., Burke, K. & Ernzerhof, M. Generalized Gradient Approximation Made Simple. *Phys. Rev. Lett.* **77**, 3865–3868 (1996).

132. Monkhorst, H. J. & Pack, J. D. Special points for Brillouin-zone integrations. *Phys. Rev. B* **13**, 5188–5192 (1976).

133. Wang, V., Xu, N., Liu, J.-C., Tang, G. & Geng, W.-T. VASPKIT: A user-friendly interface facilitating high-throughput computing and analysis using VASP code. *Comput. Phys. Commun.* **267**, 108033 (2021).

134. Togo, A., Chaput, L., Tadano, T. & Tanaka, I. Implementation strategies in phonopy and phono3py. *J. Phys. Condens. Matter* **35**, 353001 (2023).

135. Togo, A., Chaput, L., Tanaka, I. & Hug, G. First-principles phonon calculations of thermal expansion in Ti 3 SiC 2 , Ti 3 AlC 2 , and Ti 3 GeC 2. *Phys. Rev. B* **81**, 174301 (2010).

136. Blanco, M. A., Francisco, E. & Luaña, V. GIBBS: isothermal-isobaric thermodynamics of solids from energy curves using a quasi-harmonic Debye model. *Comput. Phys. Commun.* **158**, 57–72 (2004).

137. Liu, B., Wang, J. Y., Li, F. Z. & Zhou, Y. C. Theoretical elastic stiffness, structural stability and thermal conductivity of La2T2O7 (T=Ge, Ti, Sn, Zr, Hf) pyrochlore. *Acta Mater.* **58**, 4369–4377 (2010).

138. Zhong, L., Wang, Y., Luo, H., Luo, C. & Peng, J. Evolution of the microstructure, texture and thermal conductivity of as-extruded ZM60 magnesium alloy in pre-compression. *J. Alloys Compd.* **775**, 707–713 (2019).

139. Shahil, K. M. F. & Balandin, A. A. Thermal properties of graphene and multilayer graphene: Applications in thermal interface materials. *Solid State Commun.* **152**, 1331–1340 (2012).

140. Trnovcová, V., Furár, I. & Hanic, F. Influence of technological texture on electrical properties of industrial ceramics. *J. Phys. Chem. Solids* **68**, 1135–1139 (2007).

141. Hu, Y. L. *et al.* First-principle calculation investigation of NbMoTaW based refractory high entropy alloys. *J. Alloys Compd.* **827**, 153963 (2020).

142. Zhang, J., Zhang, H., Xiong, J., Chen, S. & Zhang, G. Tuning lattice thermal conductivity in NbMoTaW refractory high-entropy alloys: Insights from molecular dynamics using machine learning potential. *J. Appl. Phys.* **136**, 155106 (2024).

Acknowledgments

This work was supported by the National Natural Science Foundation of China under Grant Nos. 12275055.

Author contributions

Z.X.: Conceptualization, Methodology, Validation, Writing – original draft, Data curation, Investigation, Writing – review & editing; J.C.: Methodology, Validation, Data curation, Investigation, Writing – review & editing; J.Y.: Data curation,Writing – review & editing; Z.L.: Investigation, Writing – review & editing; F.Y.: Writing – review & editing; R.S.:Validation; H.Z.: Validation, Supervision; Y.W.: Conceptualization, Writing – review & editing, Supervision.

Competing Interests

The authors declare that they have no known competing financial interests or personal relationships that could have appeared to influence the work reported in this paper.

Additional information

Supplementary information The online version contains supplementary material available at ((will be filled in after uploading)).

Figure captions

Fig. 1 | Schematic of high-entropy alloys (HEAs) property prediction, composition optimization workflow and Target Space Partitioning-based Prediction Enhancement Strategy (TSPPES).

(a) Applying the graph neural network and multilayer perceptron (GNN–MLP) joint model to predict the bulk modulus and lattice thermal conductivity of novel HEAs, and combining Non-dominated Sorting Genetic Algorithm II (NSGA-II) and Bayesian optimization (BO) to screen for alloy composition combinations with both high performance of two properties. (b) Partitioning-based prediction identifies high-performance subspaces in the target space, potentially enabling superior model extrapolation capabilities within these regions, while simultaneously maintaining maximum element coverage (predicting bulk modulus for example in this figure).

Fig. 2 | Mix-GNN architecture, feature analysis, model performance and computational efficiency.

(a) Network of MLP branch. (b) Network of GNN branch. (c) Network of mix layers. (d) Bulk modulus feature importance (for continuous features) expressed using the Pearson correlation coefficient. (e) Lattice thermal conductivity feature importance (for continuous features) expressed using the Pearson correlation coefficient. (f) Bulk modulus and shear modulus models' performance in validation set. (g) Lattice thermal conductivity model's performance in validation set. (h) Comparisons of additional

training data required. (i) Elemental coverage. (j) Reported full-space search time.

Fig. 3 | Partitioning-based predictions and model performance in each subspace.

(a) The partitioning-based prediction of the bulk modulus model ultimately identified quinary FCC and BCC structures as the target subspace. (b) The partitioning-based prediction of the lattice thermal conductivity model ultimately identified quinary FCC and BCC structures as the target subspace.

Fig. 4 | Element-resolved marginal distributions of the optimized quinary alloys.

(a) Multi-objective optimization of bulk modulus (B) and lattice thermal conductivity (κ_l) for BCC single-phase solid solutions. (b) Multi-objective optimization of B and κ_l for FCC single-phase solid solutions. Each circle stands for one alloy composition, and internal sector color and area fraction reflect elemental atomic ratios. Element color mapping is marked in the legend. Experimentally validated alloys are highlighted with black rings.

Fig. 5 | Microstructural, compositional, and mechanical characteristics of the Pt-1, RE-3, and RE-4 alloys.

(a) X-ray diffraction (XRD) patterns of as-cast Pt-1, RE-3 and RE-4, with dominant and minor phases indexed. (b–d) Scanning electron microscopy (SEM) images and energy-dispersive X-ray spectroscopy (EDS) maps showing grain morphologies and elemental segregation. (e–h) Representative load–indentation-depth curves and indentation

morphologies. (i) Small-punch test (SPT) curves of 0.5-mm-thick Pt-1 and RE-4 specimens at room temperature, showing the larger fracture deflection of Pt-1.

Fig. 6 | Model validation across alloy families and within-system composition variations. (a) Predicted bulk-modulus (B) changes caused by Mo, Ta or Zr in a refractory system, compared with reported yield-strength (YS) changes. (b) Phase-weighted lattice thermal conductivity (κ_l) of $Al_xCoCrFeNi$ versus the experimental trend. (c) Predicted bulk-modulus-to-density ratio (B/ρ) of three lightweight systems versus literature Young's-modulus-to-density ratio (E/ρ) trends. (d) Predicted bulk-modulus response to Ta + W additions in $VCrFeTa_xW_x$ versus the literature hardness trend. (e) Experimental hardness and total thermal conductivity of the present alloys compared with representative alloy families. (f) Predicted bulk modulus and lattice thermal conductivity across six alloy families. Model predictions were calibrated using the validated subspaces; error bars denote standard deviations across independent random configurations.

Fig. 7 | Composition–property relationships and physical mechanisms in the W–Mo–Nb system.

(a–f) Ternary maps of W–Mo–Nb body-centered cubic (BCC) solid solutions showing weighted melting point, integrated crystal orbital Hamilton population (ICOHP) bonding strength, lattice distortion, equilibrium lattice constant, bulk modulus (B) and lattice thermal conductivity (κ_l). The red and blue stars mark the maximum-B and minimum-κ_l regions, respectively; dashed circles mark the extreme regions expected from lattice

distortion alone. Their spatial offsets reveal the competition among lattice distortion, bonding strength, and bond density.

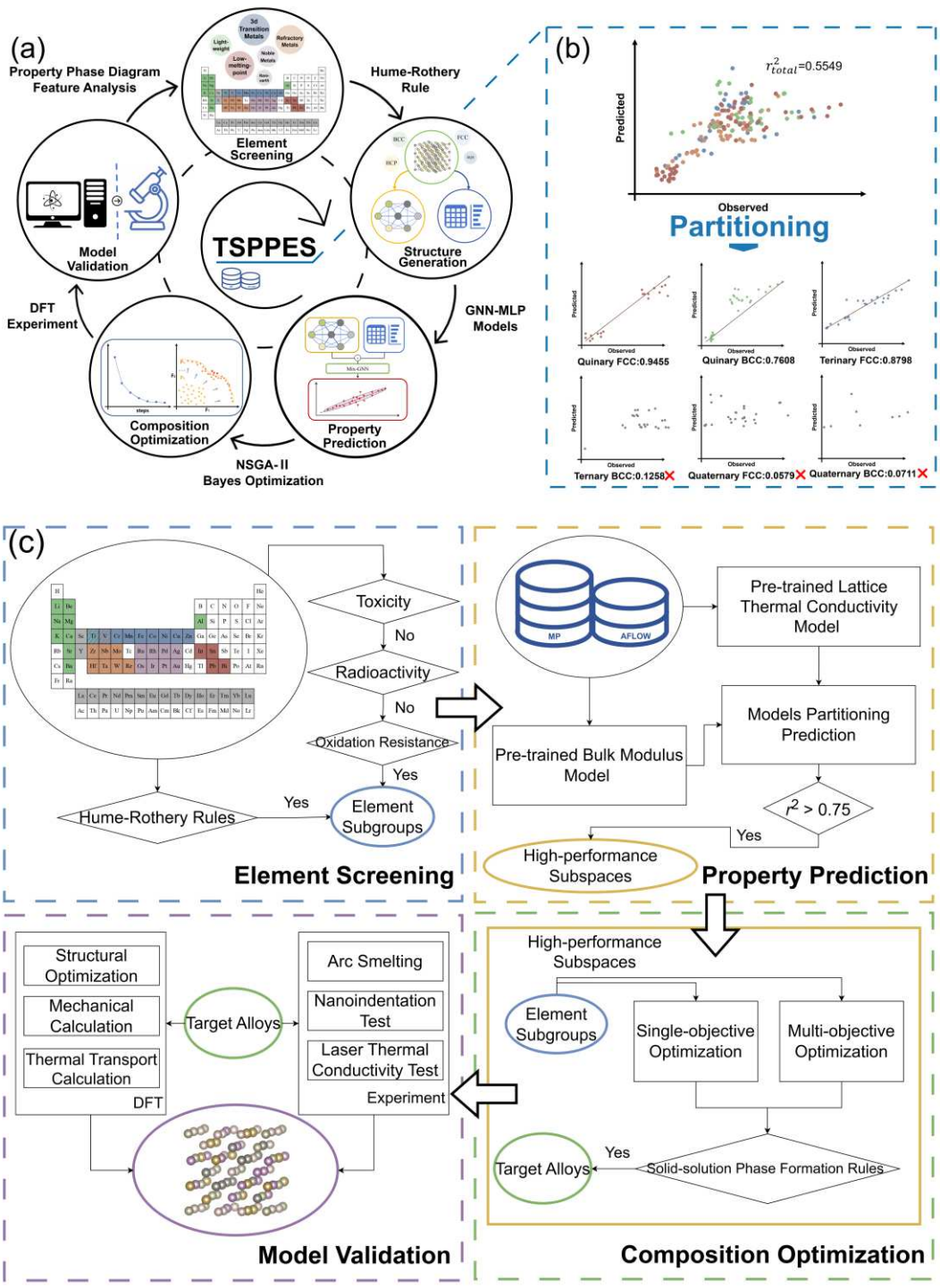


Fig. 1 Zhen Xie *et al.*

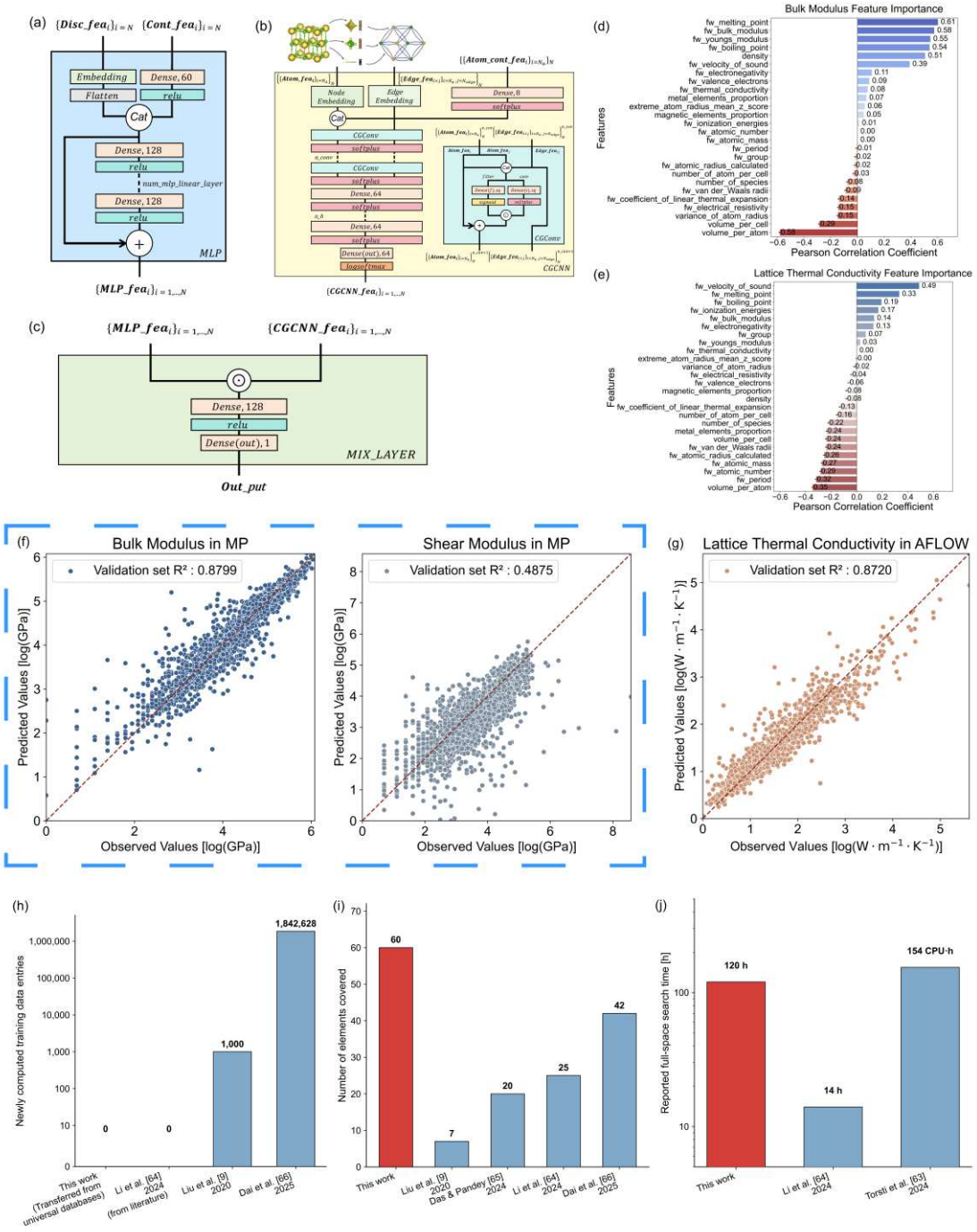
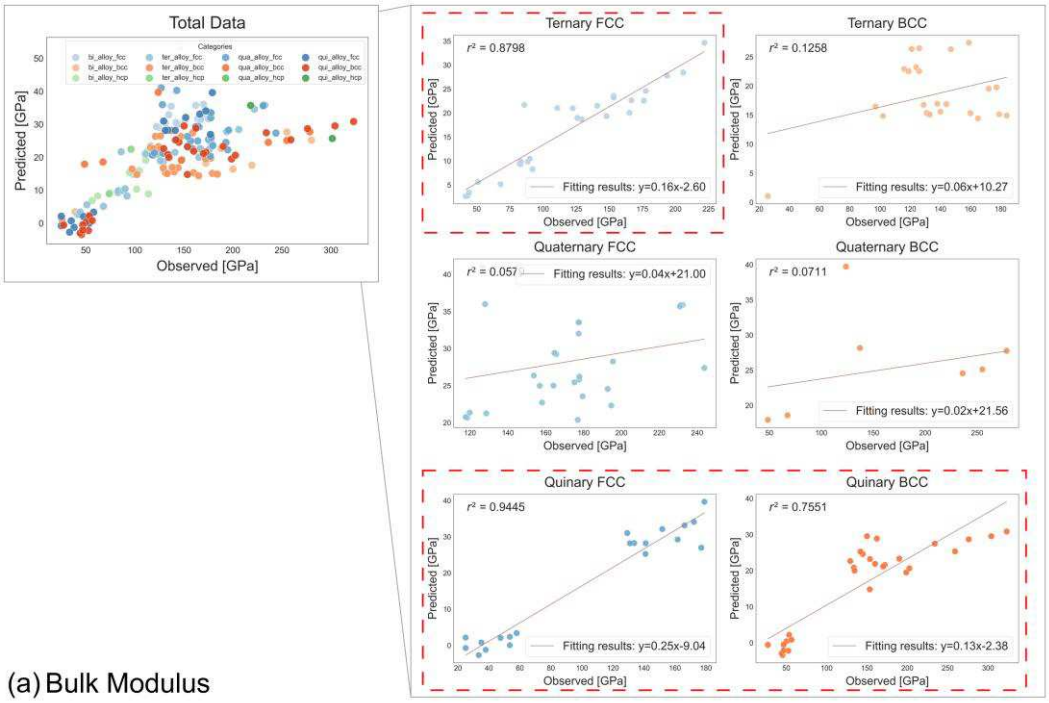
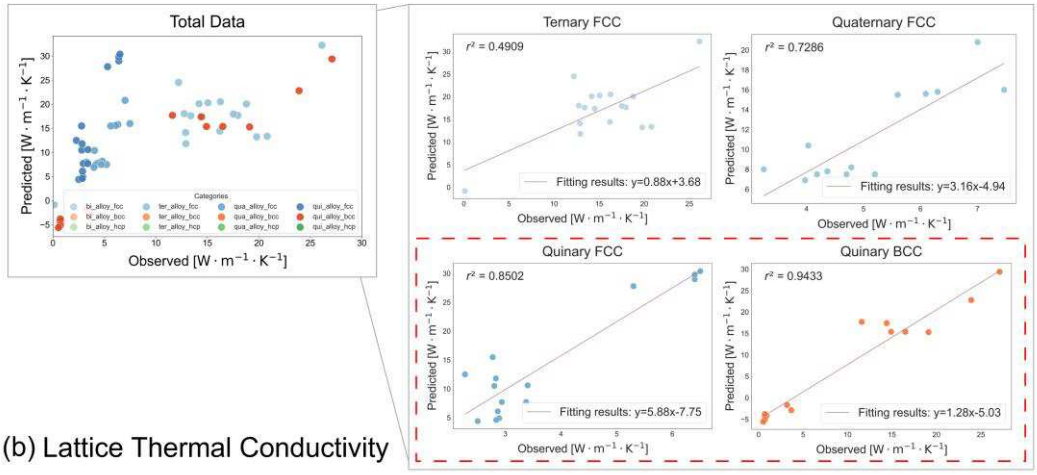


Fig. 2 Zhen Xie *et al.*



(a) Bulk Modulus



(b) Lattice Thermal Conductivity

Fig. 3 Zhen Xie *et al.*

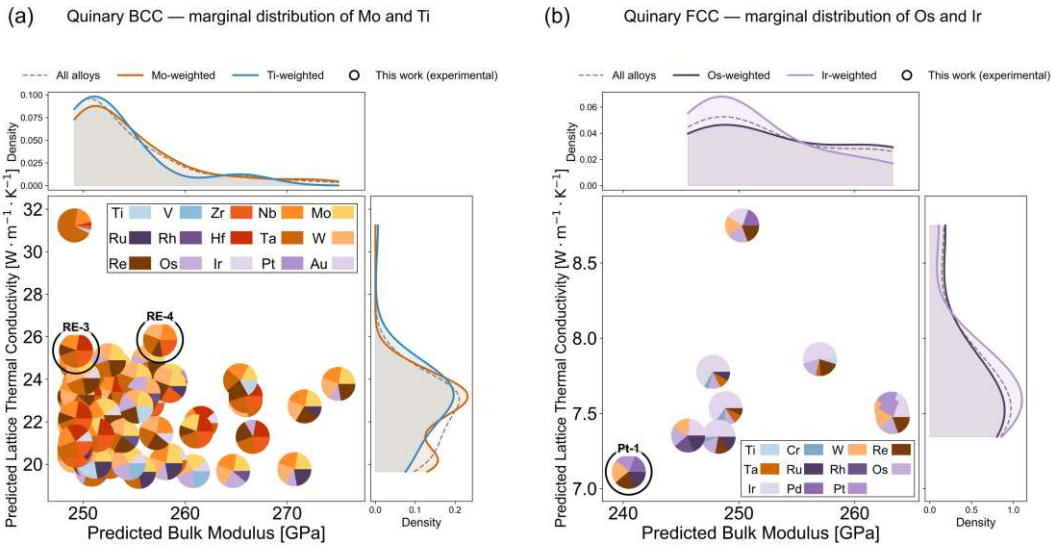


Fig. 4 Zhen Xie *et al.*

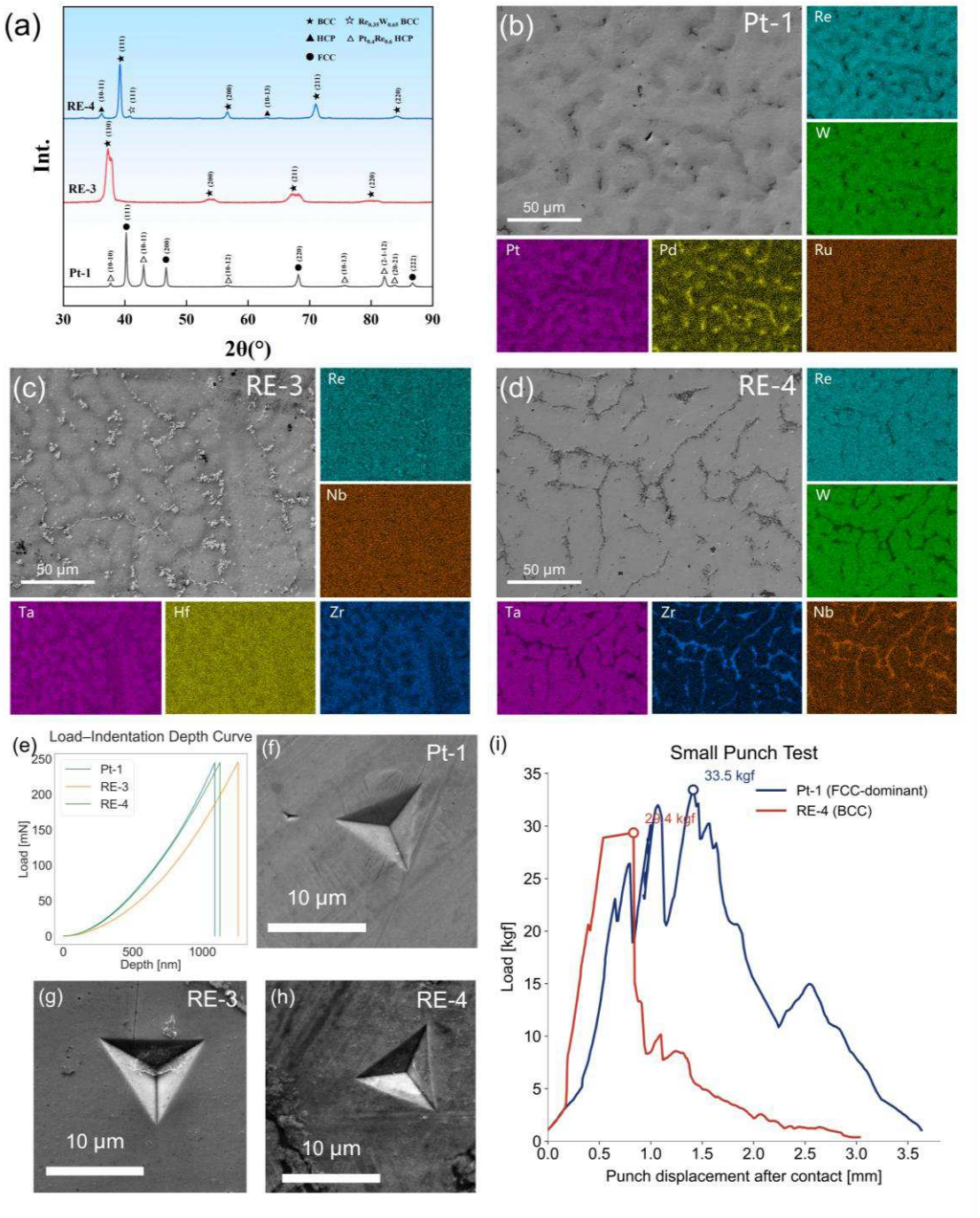


Fig. 5 Zhen Xie *et al.*

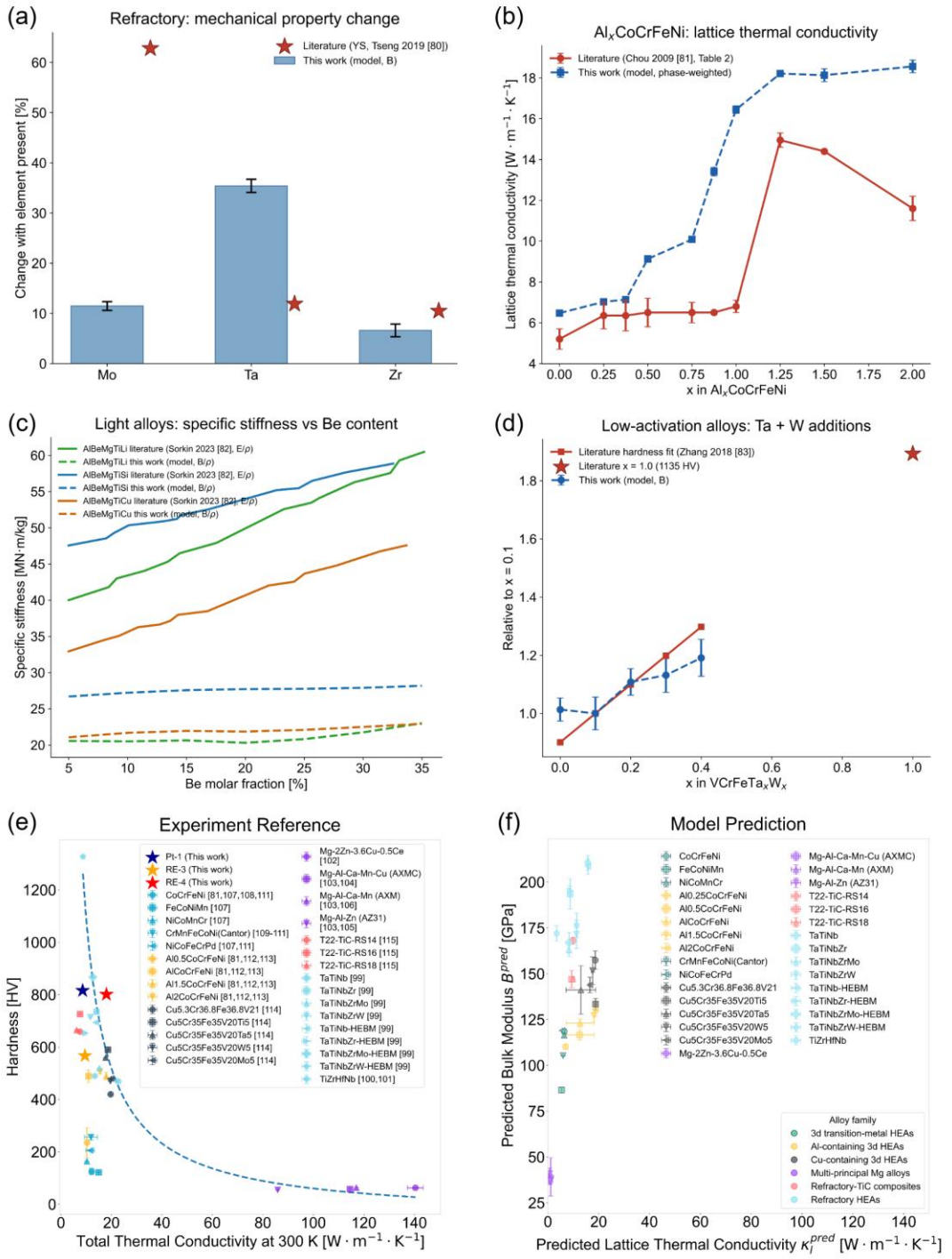


Fig. 6 Zhen Xie *et al.*

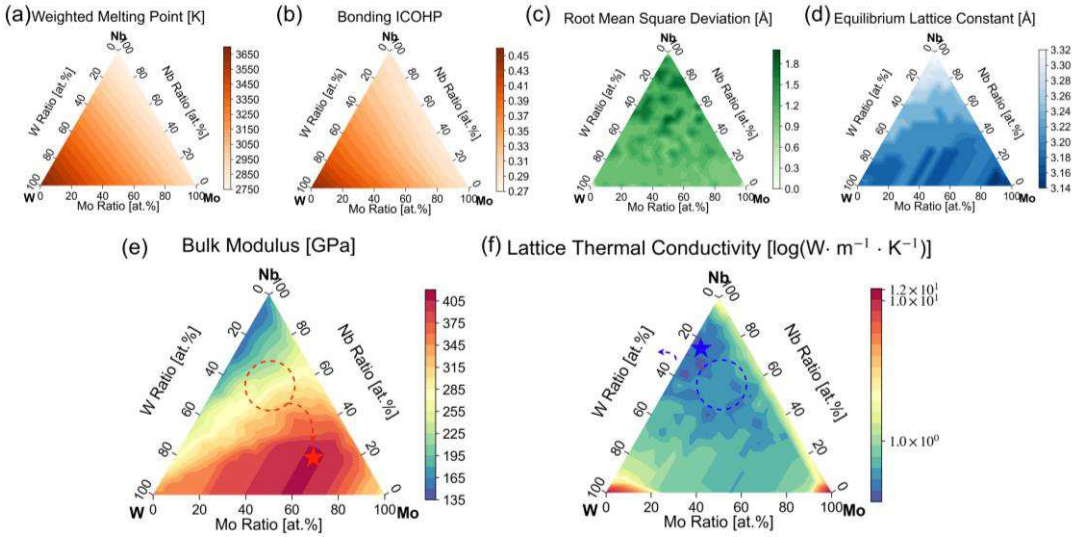


Fig. 7 Zhen Xie *et al.*

Table captions

Table 1 | The optimized high entropy alloys (HEAs) in literature and their hardness [26-34].

Table 2 | Hyperparameters of the Mix-GNN framework.

Table 3 | Candidate groups for composition optimization.

Table 4 | Single-phase high-hardness HEAs from density functional theory (DFT) calculations.

Table 5 | DFT results of single-phase high-hardness and lattice thermal conductivity HEAs.

Table 6 | Summary of lattice constants and relative deviations for the three target alloys.

Table 7 | Summary of hardness and total thermal conductivity for the three target alloys.

Table 1 | The optimized high entropy alloys (HEAs) in literature and their hardness [26–34].

Alloy composition with max hardness [*wt*.%]	Hardness [HV]	Ref.	Publication time	Data sources	Synthetic approach (if from experiment)
$Co_{26.69}Cr_{35.33}Fe_{8.05}Ni_{6.04}Al_{23.88}$	883 ± 47	[26]	12 March 2019	Experiment	Arc-melting
$Al_{40.95}Co_{23.78}Cr_{20.48}Cu_{5.98}Fe_{6.83}Ni_{5.98}$	883 ± 22	[26]	12 March 2019	Experiment	Arc-melting
$Co_{19.44}Cr_{6.67}Fe_{35.83}Ni_{5.38}V_{32.68}$	1148	[27]	1 November 2021	Experiment	Arc-melting
$Co_{14.86}Fe_{14.49}Ni_{15.18}Al_{17.31}Cr_{16.22}Mo_{21.52}Ti_{0.41}$	941 ± 13	[28]	22 July 2023	Experiment	Arc-melting
$Al_{26.70}Cr_{25.13}Fe_{10.89}Co_{30.54}Ni_{6.75}$	826 ± 20	[29]	7 November 2023	Experiment	High-frequency induction melting
$Co_{29.83}Cr_{17.98}Fe_{24.47}Mo_{7.48}Nb_{8.93}V_{11.31}$	838	[30]	26 September 2023	Experiment	Arc-melting
$Fe_{4.93}Co_{20.44}Ni_{9.78}Cr_{28.48}Al_{2.44}Ti_{33.93}$	890 ± 12	[31]	18 June 2024	Experiment	Arc-melting
$Ni_{46.00}Cr_{13.11}Al_{2.40}Co_{22.37}W_{4.83}Mo_{2.07}Ti_{4.35}Ta_{2.80}Nb_{1.90}$	487	[32]	7 June 2021	Thermo-Calc	—
$Al_{20.60}Cr_{28.35}Fe_{6.09}Co_{38.57}Ni_{6.39}$	966 ± 60	[33]	29 December 2022	ML prediction	—
$Al_{17.24}Fe_{24.79}Cr_{21.95}Mo_{6.84}Ti_{13.03}Nb_{7.89}Hf_{8.26}$	1605.66	[34]	5 March 2025	ML prediction	—
$Al_{5.70}Cr_{17.20}Mn_{8.84}Ti_{13.26}Cu_{7.83}Hf_{15.26}Si_{32.11}$	1461.21	[34]	5 March 2025	ML prediction	—

Table 2 | Hyperparameters of the Mix-GNN framework.

Module	Hyperparameters' name	The meaning of hyperparameter names	Value
Training	learning rate	—	$1e^{-3}$
	optimizer	—	Adam
	weight decay	—	$1e^{-5}$
	loss function	—	MSELoss
	batch size	—	2048
	learning rate scheduler	—	CosineAnnealingLR
	epoch	—	3000
GNN	embedding_fea_len	Size of embedding layer.	20
	continous_fea_len	Size of continuous feature input layer.	8
	atom_fea_len	Atomic feature vector size in CGConv layer.	200
	edge_fea_len	Edge feature vector size in CGConv layer.	16
	h_fea_len	Size of linear layers.	64
	n_conv	Number of CGConv layers.	4
	n_h	Number of linear layers.	2
	output_size	Size of CGCNN output layer.	80
MLP	hidden_size	Size of total hidden layer.	128
	output_size	Size of MLP output layer.	80
	num_mlp_linear_layer	Number of total linear layers.	9
	p	Dropout rate of continuous feature linear layers.	0.3
	p_total	Dropout rate of total hidden layers.	0.3
	n_linear	Number of hidden layers.	1
Mix-layer	hidden_size	Size of hidden layers.	128
	p	Dropout rate of Mix-layer.	0.6

Table 3 | Candidate groups for composition optimization.

Candidate Group	Candidate Subgroup	Elements (within 15% difference in radius from the central atom Fe, Zr, Cu, Mg and Ti)
Fe	Fe_total	Li, Mg, Ti, V, Cr, Mn, Fe, Ru, Co, Rh, Pd, Ni, Pt, Cu, Ag, Au, Zn, Ga, Sn, Sb, Bi, La
	Fe_normal	Li, Mg, Ti, V, Cr, Mn, Fe, Co, Ni, Cu, Zn, Ga, Sn, Sb, Bi
	Fe_noble	Li, Mg, Ti, V, Cr, Mn, Fe, Co, Ni, Cu, Zn, Ga, Sn, Sb, Bi, Ru, Rh, Pd, Pt, Ag, Au
	Fe_mix	Li, Mg, Ti, V, Cr, Mn, Fe, Co, Ni, Cu, Zn, Ga, Sn, Sb, Bi, Sc, Ir, Mo, W
Zr	Zr_total	Ca, Sr, Sc, Y, Ti, Zr, Hf, Nb, Ta, Mo, W, Re, Ru, Os, Ir, Pt, Nd, Eu, Gd, Tb, Dy, Er, Tm, Yb, Lu
	Zr_normal	Ca, Sr, Ti, Zr, Hf, Nb, Ta, Mo, W, Re
	Zr_noble	Ca, Sr, Ti, Zr, Hf, Nb, Ta, Mo, W, Re, Ru, Os, Ir, Pt
	Zr_rare	Ca, Sr, Sc, Y, Ti, Zr, Hf, Nb, Ta, Mo, W, Re, Nd, Eu, Gd, Tb, Dy, Er, Tm, Yb, Lu
	Zr_mix	Ca, Sr, Ti, Zr, Hf, Nb, Ta, Mo, W, Re, V, Cr, La, Pr
Cu	Cu_total	Mg, Cr, Mn, Fe, Co, Ni, Cu, Ag, Au, Zn, Ga, Ge, Sn, Sb, Bi
	Cu_normal	Mg, Cr, Mn, Fe, Co, Ni, Cu, Zn, Ga, Ge, Sn, Sb, Bi
	Cu_mix	Mg, Cr, Mn, Fe, Co, Ni, Cu, Zn, Ga, Ge, Sn, Sb, Bi, Li, Pd, Al, La
Mg	Mg_total	Mg, Cr, Fe, Co, Ni, Cu, Ag, Zn, Ga, Ge, Sn, Sb, Bi
	Mg_normal	Mg, Cr, Fe, Co, Ni, Cu, Zn, Ga, Ge, Sn, Sb, Bi
	Mg_mix	Mg, Cr, Fe, Co, Ni, Cu, Ag, Zn, Ga, Ge, Sn, Sb, Bi, Li, V, Mn, La, Al
Ti	Ti_total	Li, Ca, Sc, Ti, V, Nb, Ta, Cr, Mo, W, Mn, Re, Fe, Ru, Os, Co, Rh, Pd, Ir, Pt, Ag, Au, La
	Ti_normal	Li, Ca, Ti, V, Nb, Ta, Cr, Mo, W, Mn, Re, Fe, Co
	Ti_noble	Li, Ca, Ti, V, Nb, Ta, Cr, Mo, W, Mn, Re, Fe, Co, Ru, Os, Rh, Pd, Ir, Pt, Ag, Au
	Ti_rare	Li, Ca, Sc, Ti, V, Nb, Ta, Cr, Mo, W, Mn, Re, Fe, Co, La
	Ti_mix	Li, Ca, Ti, V, Nb, Ta, Cr, Mo, W, Mn, Re, Fe, Co, Mg, Zr, Hf, Ni, Cu, Sn, Bi, Nd

Table 4 | Single-phase high-hardness HEAs from density functional theory (DFT) calculations.

Alloy ID	Formula[a)]	Predicted *B* [GPa]	Calculated *B* [GPa]	Calculated *G* [GPa]	Calculated *Hv* [HV][b)]	Pugh's Ratio[c)]	Poisson's Ratio
Benchmark-1	WC ($P\bar{6}m2$)	—	380 [56]	263 [56]	3084 [73]	1.44	0.22 [56]
Benchmark-2	W ($Im\bar{3}m$,single crystal)	—	302 [56]	148 [56]	1352.85 [56]	2.04	0.29 [56]
FCC-1	$W_{21}Re_{21}Pt_{24}Ir_{21}Os_{21}$	263.54	352.80	190.92	1923.45	1.85	0.271
FCC-2	$W_{21}Re_{21}Pt_{24}Ir_{21}Ru_{21}$	254.08	339.59	176.16	1732.64	1.93	0.280
FCC-3	$Re_{21}Pt_{24}Ir_{21}Ru_{21}Mo_{21}$	242.64	328.79	175.27	1780.60	1.88	0.274
FCC-4	$Pt_{21}Ru_{21}Pd_{21}Ag_{21}Au_{24}$	203.34	210.81	73.14	589.42	2.88	0.346
BCC-1	$W_{10}Re_{10}Ir_{14}Nb_{10}Mo_{10}$	311.54	299.87	107.31	801.12	2.79	0.340
BCC-2	$W_{10}Re_{10}Ru_{14}Ta_{10}Mo_{10}$	283.54	281.48	91.82	644.89	3.23	0.35
BCC-3	$W_{12}Os_{12}Ir_{6}Nb_{12}Mo_{12}$	300.31	287.34	123.57	1008.97	2.33	0.312
BCC-4	$W_{15}Re_{10}Ir_{4}Os_{10}Mo_{15}$	285.54	323.63	84.23	482.65	3.84	0.379
BCC-5	$Re_{10}Pt_{3}Ir_{5}Os_{5}Mo_{31}$	281.23	312.03	98.89	702.04	3.16	0.359
BCC-6	$Mo_{14}Zr_{10}Hf_{10}Ta_{10}Nb_{10}$	253.69	175.52	42.35	264.98	4.14	0.389
BCC-7	$Mo_{6}Zr_{12}Hf_{12}Ta_{12}Nb_{12}$	290.23	153.59	38.42	258.03	4.00	0.387

[a)] The subscripts represent the number of atoms of each element in the 108-atom (FCC) and 54-atom (BCC) supercell; [b)] The Vickers hardness values were estimated using the shear modulus according to the formula in reference [73]. Since there is no definitive conversion table available for the unit conversion of micro-Vickers hardness in HEAs, the Vickers hardness values in GPa were multiplied by 102.04 as per conventional practice to obtain the estimated values in HV; [c)] When the Pugh's ratio (B/G) exceeds 1.75, the material exhibits ductility [97].

Table 5 | DFT results of single-phase high-hardness and lattice thermal conductivity HEAs.

Alloy ID	Formula	Predicted B [GPa]	Calculated B [GPa]	Calculated Hv [HV]	Pugh's Ratio	Predicted κ_l [W·m^{-1}·K^{-1}]	Calculated κ_l [W·m^{-1}·K^{-1}]
Benchmark-1	W ($Im\bar{3}m$,single crystal)	—	302 [56]	1352.85 [56]	2.04	—	46 [86]
Benchmark-2	NbMoTaW	—	247 [141]	796.21 [141]	2.42	—	1.72 [142]
FCC-1	$W_{24}Re_{21}Pt_{21}Pd_{21}Ru_{21}$	235.93	306.94	1332.65	2.14	7.09	6.62
FCC-2	$W_{21}Re_{21}Pt_{24}Os_{21}Ir_{21}$	263.54	352.80	1923.45	1.85	7.52	8.44
FCC-3	$W_{21}Re_{21}Os_{21}Ir_{24}Pd_{21}$	250.28	336.13	1747.03	1.91	8.68	8.33
FCC-4	$W_{27}Re_{27}Pt_{27}Pd_{27}$	257.26	300.02	1172.04	2.27	7.02	6.01
FCC-5	$W_{27}Re_{27}Ir_{6}Pd_{48}$	248.47	285.05	965.91	2.48	7.80	6.46
FCC-6	$W_{27}Re_{27}Ir_{6}Ru_{48}$	262.51	348.58	1599.51	2.04	10.72	10.23
BCC-1[a)]	$Re_{13}Mo_{5}Ta_{12}Zr_{12}Nb_{12}$	259.03	265.20	1585.26	1.72	25.95	9.80
BCC-2	$Re_{13}Mo_{5}Ta_{12}V_{12}Nb_{12}$	259.34	265.20	1653.02	1.70	26.60	16.31
BCC-3	$Re_{6}Hf_{12}Ta_{12}Zr_{12}Nb_{12}$	254.31	163.65	708.57	2.36	25.42	13.51
BCC-4	$W_{12}Re_{6}Ta_{12}Zr_{12}Nb_{12}$	262.70	219.97	1131.79	2.06	25.93	15.03
BCC-5	$W_{5}Ta_{12}Mo_{13}Hf_{12}Nb_{12}$	284.09	216.50	927.26	1.98	22.94	10.01
BCC-6	$Re_{12}Ta_{12}Mo_{9}Nb_{12}Ti_{9}$	270.66	254.69	1473.12	1.73	24.02	11.21

[a)] Due to the instability of BCC-1~6 crystal modeled by SQS method, before calculating the mechanical properties and lattice thermal conductivity, Metropolis Monte Carlo algorithm is used to search for the low-energy stable short-range order (SRO) structure with the same composition at 300 K, and then the mechanical and thermal transport properties are further calculated.

Table 6 | Summary of lattice constants and relative deviations for the three target alloys.

Sample	Alloy composition [*wt.*%]	Theoretical lattice constan [Å]	Experimental lattice constant [Å]	Deviation [%]
Pt-1	$W_{18.74}Re_{22.31}Pt_{31.55}Pd_{15.30}Ru_{12.10}$	3.895	3.891	0.103
RE-3	$Re_{14.62}Hf_{28.05}Ta_{28.42}Zr_{14.33}Nb_{14.58}$	3.356	3.378	0.651
RE-4	$W_{28.63}Re_{14.50}Ta_{28.18}Zr_{14.21}Nb_{14.47}$	3.234	3.248	0.431

Table 7 | Summary of hardness and total thermal conductivity for the three target alloys.

Sample	Theoretical *Hv* [HV]	Experimental *Hv* [HV]	Hardness ratio (Exp./Theo.)	Theoretical κ_t [$W \cdot m^{-1} \cdot K^{-1}$]	Experimental κ_t [$W \cdot m^{-1} \cdot K^{-1}$]	κ_t ratio (Exp./Theo.)
Pt-1	1332.65	816 ± 49	61.2%	12.47	8.583 ± 0.009	68.8%
RE-3	708.57	567 ± 7	80.0%	24.68	9.519 ± 0.013	38.6%
RE-4	1131.79	801 ± 9	70.8%	30.27	18.002 ± 0.060	59.5%

Supplementary Files

This is a list of supplementary files associated with this preprint. Click to download.

- supplementaryinformation.docx